Waveshape of THz radiation produced by two-color laser-induced air plasmas

Alexandre Stathopulos, Stefan Skupin, Binbin Zhou, Peter U. Jepsen, Luc Bergé

To cite this version:

Alexandre Stathopulos, Stefan Skupin, Binbin Zhou, Peter U. Jepsen, Luc Bergé. Waveshape of THz radiation produced by two-color laser-induced air plasmas. Physical Review Research, 2024, 6, pp.043274. 10.1103/PhysRevResearch.6.043274 . hal-04625038v2

HAL Id: hal-04625038
https://hal.science/hal-04625038v2

Submitted on 17 Dec 2024

PHYSICAL REVIEW RESEARCH **6**, 043274 (2024)

Waveshape of terahertz radiation produced by two-color laser-induced air plasmas

A. Stathopulos,[1,2] S. Skupin,[3] B. Zhou,[4] P. U. Jepsen,[4] and L. Bergé[5,*]
[1]*CEA, DAM, DIF, 91297 Arpajon, France*
[2]*Université Paris-Saclay, CEA, LMCE, 91680 Bruyères-le-Châtel, France*
[3]*Institut Lumière Matière, UMR 5306 - CNRS, Université de Lyon 1, 69622 Villeurbanne, France*
[4]*DTU Electro - Department of Electrical and Photonics Engineering, Technical University of Denmark, 2800 Kongens Lyngby, Denmark*
[5]*Centre des Lasers Intenses et Applications, Université de Bordeaux-CNRS-CEA, 33405 Talence Cedex, France*

(Received 19 June 2024; accepted 4 November 2024; published 13 December 2024)

The spatial and spectral distributions of terahertz (THz) pulses emitted by two-color air plasmas are theoretically investigated for focused laser pulses and in the filamentation regime. We derive a so-called *augmented* conical emission model, which, like the one proposed by You *et al.* [Phys. Rev. Lett. **109**, 183902 (2012)], involves phase matching between laser harmonics along the plasma channel, the plasma density and length, and the emitted frequency as key parameters. Our augmented model, however, treats envelope effects and accounts for transverse variations of both plasma- and Kerr-driven potential THz emitters. We highlight the importance of the characteristic spatiospectral distributions of these two conversion mechanisms in the expression of the angular radiated power. The results of our model are successfully compared with data provided by a comprehensive, fully space- and time-resolved unidirectional solver. Importantly, these numerical simulations clear up the effective plasma length along which THz emission develops, compared with the dephasing length over which the laser fundamental and second harmonic shift out-of-phase. The impact of common optical aberrations, such as sphericity, astigmatism, and coma, on the THz generation is also investigated. Aberrations are shown to generally decrease the laser-to-THz conversion efficiency and potentially induce spatial asymmetries and narrowing of the THz spectra.

DOI: 10.1103/PhysRevResearch.6.043274

I. INTRODUCTION

The production of terahertz (THz) radiation is receiving increasing interest in a wide range of domains, such as homeland security [1–3], medical diagnosis [4–6], art conservation [7–10], and archeology [11,12]. THz waves can propagate through a few millimeters of optically opaque materials, provided the water concentration is low [13,14], and can be used to identify complex molecules by coherent THz spectroscopy [15–18]. Other notable applications of THz waves include control of leaf water content [19–21], plasma excitation [22], electron acceleration [23], high harmonic (sideband) generation [24–26], and the fabrication of ferromagnetic structures [27]. Several emitters can produce intense pulsed or continuous-wave THz radiation, including photoconductive antennas [28,29], molecular (CH_3OH) gas sources [30], quantum cascade lasers [31–33], and $\chi^{(2)}$ crystals that serve for optical rectification [34]. However, THz time-domain spectroscopy (THz-TDS) requires broadband THz radiation to access extended absorption spectra, allowing the identification of molecules or precise determination of the physics of broadband processes such as relaxation and conductivity. This need can be fulfilled by ionizing a gas with an ultrashort multicolor laser pulse. This method generates strong ($\sim$0.1–1 GV/m) and ultrabroadband (>100 THz) THz fields with significant conversion efficiencies ($>10^{-4}$) [35,36]. Another benefit of this technique is the nondestructive nature of the mechanisms at play, e.g., in air plasmas. The laser driver usually comprises only two harmonics. However, recent theoretical and experimental studies have shown that adding more harmonics to the optical beam can dramatically increase the THz yield [37–41].

When a temporally asymmetric femtosecond light pulse composed of a fundamental component and its second harmonic reaches the $\sim 10^{14}\ \mathrm{W/cm^2}$ intensity range, sufficient to photoionize a gas (here ambient air) [42], an underdense plasma is created. The electrons freed by this process are then accelerated by the asymmetric laser field and induce a photocurrent that contains a low-frequency component. This quasi-DC contribution causes the plasma to radiate in the THz domain. Although this process is usually exploited in the so-called *focused regime*, where a plasma spot is formed a few tens of centimeters after a focusing element (converging lens or mirror), its efficiency was also confirmed in the long-range *filamentation regime* [43] that results from a sequence of local equilibria between Kerr self-focusing and plasma defocusing maintained over meter-long distances [44]. This second regime, which usually requires to operate in loosely focused ($\sim$1 m focal lengths) or collimated beam propagation

---

[*] Contact author: luc.berge@u-bordeaux.fr

geometry, could be advantageous for THz-TDS of explosives for safety reasons [45,46].

One specificity of THz wave generation by two-color air plasmas is the typically conical shape of the THz radiation [47]. In their seminal work, You *et al.* [48] and Oh *et al.* [49] advocated that conical emission is due to interferences between the THz waves produced at different places along a generated cylindrical homogeneous plasma, as their polarity changes with the phase angle between the two laser harmonics caused by optical and plasma dispersion. Importantly, the key parameters driving THz emission in this scenario are the plasma length L, over which THz emission takes place, and the dephasing length l_d, over which the two pump harmonics shift out of phase. The latter length depends on the plasma density N_e. Other models describing the angular THz power spectrum have been elaborated in the literature; most of them also assume a homogeneous plasma cylinder [50,51]. Although these assumptions are generally met, in practice, optical beam distortions are always present. They can affect the stability and symmetry of the emitter, thereby degrading the generated THz radiation. An alternative theory [52] tried to account for the role of plasma opacity, relevant for THz frequencies lower than the local plasma frequency, as well as oblique diffraction of THz waves through a transversally varying plasma channel and the spectral sensitivity of the experimental detector. Although showing reasonable agreement between semianalytical results and experimental measurements, the authors do not share enough information about key parameters in THz emission (selected THz frequencies, plasma profiles, or the experimental detector frequency responses) to provide an accurate and convincing model for conical emission. They claim the emission is always conical. At the same time, one of the remaining problems to date is the seemingly generic coexistence of on-axis emission at low frequencies ($\lesssim 5$ THz) with a donut-shaped emission at large THz frequencies (> 5 THz) in focused propagation [47,53–55].

In this paper, we address this open question and more generally aim at clarifying the THz spectral dynamics for the two propagation regimes of interest mentioned above, namely, a focused propagation producing short, cm-long plasma channels and an extended filamentation regime producing meter-range plasma channels. Because the model of You *et al.* [48] cannot account for the effects of transverse variations in the THz emitter profile, we propose a so-called *augmented model* conveying this information through the transverse spatial Fourier transform of both the electron current density and the nonlinear (Kerr) polarization. To test our model, we investigate the effects of common optical aberrations (OAs) on the THz emission. In both propagation regimes, a rigorous comparison is performed between the model of You *et al.* [48], our augmented model, and comprehensive three-dimensional (3D) numerical simulations. We show that, while the model of You *et al.* [48] describes the main features of the conical emission, the augmented model better reproduces the THz emissions for a transversely modulated laser beam phase, from a simple focusing lens to more complex optical abberations. Last but not least, we demonstrate that following the spectral dynamics along the length of the generated plasma channel explains the abovementioned coexistence of on-axis and conical emission in the focused propagation regime.

This paper is organized into three parts. Section II introduces the underlying physics of THz generation, mainly dominated by photocurrents. It also recalls the 3D unidirectional pulse propagation equation (UPPE) [56] and the so-called local current (LC) model [50,57] that is extended to include the instantaneous Kerr response. In Sec. III, we establish the augmented THz emission model that keeps the key ingredients of the theory developed by You *et al.* [48] but accounts for (i) the spectral distributions characterizing the propagation regimes through the baseline configurations marked by different interplays between photocurrents and Kerr effect, (ii) transverse variations in the emitting source induced by laser spatial inhomogeneities or a simple linear focusing phase, and (iii) optical envelope profiles and changes in the laser polarization state, e.g., from linear to circular. Results obtained from this augmented model are compared with the THz spatiospectral distributions provided by vectorial full space- and time-resolved UPPE simulations. As our model considers transverse distortions in the laser pulse wavefront, Sec. IV is dedicated to the influence of common OAs on laser propagation, plasma geometry, and THz radiation. We model OAs using Zernike polynomials that affect the input pulse phase [58]. We then compare the resulting angular THz spectra evaluated by our semianalytical model with UPPE simulation results for the most common OAs in laser experiments: sphericity, astigmatism, and coma. Section V concludes this work.

II. PHYSICAL MECHANISM FOR THz GENERATION AND LASER PROPAGATION MODEL

We study the THz emission by two-color femtosecond light pulses that trigger air plasmas. The laser field can be either linearly polarized along the x axis when the two harmonics are oriented along the same transverse direction [linear polarization–parallel (LP-P)] or circularly polarized when the colors are circularly polarized and both rotate in the same direction [circular polarization–same (CP-S)]. Authors of previous works [59,60] have reported that CP-S laser pulses can increase by a factor ∼4–6 the laser-to-THz conversion efficiency compared with their LP-P counterpart. The temporal profiles of the input pulse at $z = 0$ are chosen as

$$\mathbf{E}_{\text{LP-P}}(\mathbf{r}_\perp, t) = [\mathcal{E}_1 \cos(\omega_0 t) + \mathcal{E}_2 \cos(2\omega_0 t + \phi)]\mathbf{e}_x, \quad (1)$$

$$\mathbf{E}_{\text{CP-S}}(\mathbf{r}_\perp, t) = \frac{1}{\sqrt{2}}\begin{bmatrix} \mathcal{E}_1 \cos(\omega_0 t) + \mathcal{E}_2 \cos(2\omega_0 t + \phi) \\ \mathcal{E}_1 \sin(\omega_0 t) + \mathcal{E}_2 \sin(2\omega_0 t + \phi) \end{bmatrix}, \quad (2)$$

where ω_0 is the laser fundamental frequency, ϕ the phase angle between the two colors, and $\mathcal{E}_{1,2}$ their envelopes being initially Gaussian in time and space:

$$\mathcal{E}_{1,2}(\mathbf{r}_\perp, t) = \sqrt{r_{1,2}} E_0 \exp\left[-\frac{t^2}{t_{1,2}^2} - \frac{r_\perp^2}{w_{1,2}^2}\right]. \quad (3)$$

Here, E_0 is the laser amplitude, and $t_{1,2}$ and $w_{1,2}$ are the $1/e^2$ duration and width of the two harmonics. The peak intensity ratio of the fundamental to the second harmonic is determined by $r_2 = r$ and $r_1 = \sqrt{1-r}$, with $0 \leqslant r \leqslant 1$. A focusing lens with focal length f is considered by adding a phase to the input pulse in the temporal Fourier domain:

$$\widehat{\mathbf{E}}(r_\perp,\omega) \rightarrow \widehat{\mathbf{E}}(r_\perp,\omega)\exp\left(-i\frac{\omega}{c}\frac{r_\perp^2}{2f}\right). \tag{4}$$

Later in Sec. IV, the transverse spatial dependency of this phase term $\propto r_\perp^2/2f$ describing a perfect focusing lens will be generalized to an (x, y)-dependent function $Z_{\mathrm{OA}}(\mathbf{r}_\perp)$, accounting for OAs.

Photoionization caused by the laser pulse with intensity $\sim 10^{13}$–$10^{15}\,\mathrm{W/cm^2}$ takes place in the tunneling regime [42,61,62], leading to a stepwise increase in the free electron density described by the rate equation:

$$\partial_t N_e = W(E)(N_a - N_e), \tag{5}$$

where $W(E)$ is the photoionization rate, and N_a is the initial neutral density (here, written for one species for simplicity). The free electrons are then accelerated by the laser field and generate photocurrents governed for nonrelativistic plasmas by

$$(\partial_t + \nu_c)\mathbf{J}_e = \frac{e^2}{m_e}N_e\mathbf{E}, \tag{6}$$

where ν_c denotes an electron-neutral collision rate taken as $\nu_c = 2.86\,\mathrm{THz}$. Although low-frequency radiation is mainly generated from photocurrents, for weaker laser intensities ($< 10^{13}\,\mathrm{W/cm^2}$), an additional contribution to the overall THz yield may be provided by the Kerr polarization, that is, the third-order nonlinear response of the bound electrons [47,63,64], reading

$$\mathbf{P}_K(\mathbf{r},t) = \varepsilon_0\chi^{(3)}E^2(\mathbf{r},t)\mathbf{E}(\mathbf{r},t), \tag{7}$$

with $\chi^{(3)}$ being the third-order electric susceptibility [65] assumed to be nondispersive, i.e., $\chi^{(3)} \equiv \chi^{(3)}(-\omega_0,\omega_0,\omega_0)$. A second well-known action of the Kerr response is to transversally compress the laser beam. It is maintained in a self-focused state through optical self-focusing and plasma defocusing sequences as its peak power remains higher than the critical power for self-focusing [44]:

$$P_{\mathrm{cr}} \approx \frac{3.72\lambda_0^2}{8\pi n_0 n_2}, \tag{8}$$

with $n_0 = n_{\mathrm{opt}}(\omega_0)$, $n_{\mathrm{opt}}(\omega)$ denoting the linear optical refractive index of air taken from Ref. [66], and $n_2 = 3\chi^{(3)}/(4n_0^2c\varepsilon_0)$ is the nonlinear refractive index.

During propagation in air, the laser pulse can also excite rotational transitions, mostly in N_2 molecules, leading to stimulated Raman rotational scattering (SRRS) with polarization:

$$\mathbf{P}_R(t) = \frac{3}{2}x_K\varepsilon_0\chi^{(3)}\int_0^{+\infty}\mathbf{G}(\mathbf{E},t,\tau)R(\tau)d\tau. \tag{9}$$

Here, x_K is the ratio of SRRS to the total third-order response, $\mathbf{G}(\mathbf{E},t,\tau)$ is a function that describes the third-order interaction for arbitrary-polarized laser pulses established in Ref. [67], and $R(\tau)$ is the delayed Raman response function detailed in Refs. [68,69]. The ratio x_K is estimated to be $\approx 80\%$ according to Zahedpour *et al.* [70]. This delayed nonlinearity affects the laser pulse propagation and, therefore, cannot be omitted when comprehensive UPPE simulations are performed. However, as shown in Refs. [64,67], the contribution of SRRS to the overall THz yield is negligible compared with the other sources (instantaneous Kerr response and photocurrents), so only the instantaneous Kerr nonlinearity Eq. (7) weighted by the factor $(1 - x_K)$ will be considered when we further elaborate on our augmented model.

In the following, we shall perform a systematic comparison between semianalytically computed angular spectra and far-field THz spectra calculated using the UPPE [56,71]:

$$\begin{aligned}\frac{\partial\overline{\mathbf{E}}}{\partial z} &= i\sqrt{k^2(\omega) - k_\perp^2}\,\overline{\mathbf{E}}\\ &\quad + \frac{i\mu_0\omega^2}{2k(\omega)}\left[\frac{i}{\omega}(\overline{\mathbf{J}}_e + \overline{\mathbf{J}}_{\mathrm{loss}}) + \overline{\mathbf{P}}_K + \overline{\mathbf{P}}_R\right].\end{aligned} \tag{10}$$

Here, the notation

$$\begin{aligned}&\overline{f}(\mathbf{k}_\perp,\omega)\\ &\quad = \iiint_{-\infty}^{+\infty} f(\mathbf{r}_\perp,t)\exp\left(-i\mathbf{k}_\perp\cdot\mathbf{r}_\perp + i\omega t\right)d\mathbf{r}_\perp dt\end{aligned}$$

refers to the Fourier transform of any function $f(\mathbf{r}_\perp,t)$ in time and transverse variables, $\mathbf{J}_{\mathrm{loss}}$ is the loss current density associated with photoionization, and $k(\omega) = \omega n_{\mathrm{opt}}(\omega)/c$ accounts for the linear dispersion. In our analysis and simulations, the propagation medium is ambient air, composed of 20% O_2 and 80% N_2 with ionization energies $U_i = 12.1\,\mathrm{eV}$ [72] and $U_i = 15.6\,\mathrm{eV}$ [72], respectively. The initial neutral density is $N_a = 2.7\times 10^{19}\,\mathrm{cm^{-3}}$, and photoionization is modeled using the ionization rate of Perelomov, Popov, and Terent'ev (PPT) [62] with effective charge numbers $Z^*_{O_2} = 0.53$ and $Z^*_{N_2} = 0.9$ according to Talebpour *et al.* [73].

Two representative $1/e^2$ beam widths will be considered, namely, $w_{1,2} = 250\,\mu\mathrm{m}$ for spatially narrow beams and $w_{1,2} = 2.5\,\mathrm{mm}$ for broad beams. To simulate the latter in the long-range filamentation regime and save computational cost, a preprocessor was used, which integrates the linear part of Eq. (10) before reaching the electric field threshold of $\sim 1\,\mathrm{GV/m}$ ($\sim 10^{11}\,\mathrm{W/cm^2}$) above which the (Kerr) nonlinearity kicks in. Because the preprocessor solves a linear propagation equation, the solution can be obtained analytically:

$$\overline{\mathbf{E}}(\mathbf{k}_\perp,\omega,z+\Delta z) = \overline{\mathbf{E}}(\mathbf{k}_\perp,\omega,z)\exp[i\Delta z\sqrt{k(\omega)^2 - k_\perp^2}]. \tag{11}$$

Further Fourier interpolation was then carried out to refine the spatial resolution of the resulting data, which were used as initial conditions for the UPPE simulations to properly compute the subsequent nonlinear propagation. The spatial resolution used in the UPPE simulations was $\Delta x = \Delta y = 4\,\mu\mathrm{m}$ for narrow beams and $\Delta x = \Delta y = 5$–$7\,\mu\mathrm{m}$ for broad beams and up to $15\,\mu\mathrm{m}$ for the filamentation of beam profiles distorted by coma. The temporal resolution was $\Delta t = 100$ as, and a (comoving) time window of 1.5 ps guaranteed a spectral resolution of $\Delta\nu = 0.66\,\mathrm{THz}$.

In addition to performing costly UPPE simulations, we also integrated the LC model [50,57,74], which neglects propagation effects and approximates the electric field emitted by the plasma and Kerr source terms as

$$\widehat{\mathbf{E}}(\omega) \propto [-i\omega\widehat{\mathbf{J}}_e(\omega) - \omega^2\widehat{\mathbf{P}}_K(\omega)], \tag{12}$$

with $\widehat{f}(\omega)$ denoting the Fourier transform in time of $f(t)$.

III. THz EMISSION MODEL

Analytical results from the LC model provide the dependence on the phase angle ϕ of the THz amplitudes generated by photocurrents and Kerr response [60] as

$$\mathbf{E}^J_{\mathrm{THz,LP-P}} \propto \sin\phi\ \mathbf{e_x}, \qquad \mathbf{E}^K_{\mathrm{THz,LP-P}} \propto \cos\phi\ \mathbf{e_x}, \tag{13}$$

$$\mathbf{E}^J_{\mathrm{THz,CP-S}} \propto \begin{pmatrix}\sin\phi\\ \cos\phi\end{pmatrix}, \qquad \mathbf{E}^K_{\mathrm{THz,CP-S}} \propto \begin{pmatrix}\cos\phi\\ -\sin\phi\end{pmatrix}. \tag{14}$$

Here, E^J_{THz} and E^K_{THz} are the THz electric fields produced by the photocurrents (index J) and Kerr response (index K) of LP-P and CP-S pump pulses, respectively. In practice, plasma channels extend over millimeter to centimeter lengths in the focused regime and up to several meters in the (collimated or loosely focused) filamentation regime. Over sufficiently long propagation ranges, the optical and plasma dispersion induce an important variation of the phase ϕ along the plasma channel, i.e., for an axially homogeneous plasma:

$$\phi(z) = \phi_0 + \pi\frac{z}{l_d}, \tag{15}$$

where ϕ_0 is the phase angle taken at the plasma onset distance. The dephasing length l_d represents the propagation distance over which ϕ changes by π due to dispersion, that is,

$$l_d = \frac{\lambda_0}{4\mathrm{Re}[n(2\omega_0) - n(\omega_0)]}, \tag{16}$$

with $\lambda_0 = 2\pi c/\omega_0$, and Re denotes taking the real part of a complex number. Here, $n(\omega)$ is the medium refractive index that accounts for the contributions of Kerr and plasma:

$$n^2(\omega) = n^2_{\mathrm{opt}}(\omega) + 2n_0n_2I_0 - \frac{\omega_p^2}{\omega^2(1 + i\nu_c/\omega)}, \tag{17}$$

where $I_0 = c\varepsilon_0 n_0 E_0^2/2$ is the incident pulse intensity, and $\omega_p = \sqrt{e^2N_e/\varepsilon_0 m_e}$ is the electron plasma frequency. Here, we recall that l_d depends on N_e through the plasma frequency in Eq. (17). Note the difference by a factor of 2 with the definition of the dephasing length of You *et al.*, which is due to a misprint in the original Ref. [48].

A. Conical emission model of You *et al.* [48]

Before dwelling upon our revised model, we find it instructive to recall the main ingredients of the theory of You *et al.* [48] (see also Oh *et al.* [49]) that describes the THz intensity radiated in the far-field by a homogeneous ($N_e = \mathrm{const.}$) cylindrical plasma of length L and radius a. Here, the only mechanism generating THz waves is the photocurrent density excited by an LP-P laser pulse, and thus, according to Eq. (13), the local THz amplitude evolves as $\sin\phi(z)$. Derived from the radiated electric field in the far-field approximation, You *et al.* [48] obtained the angular THz intensity spectrum (see the Appendices for a detailed derivation):

$$|\widehat{E}(\omega_{\mathrm{THz}}, \Theta)|^2 \propto |A(\omega_{\mathrm{THz}})|^2\left[\frac{J_1(\beta)}{\beta}\right]^2 \times L^2[\kappa_+^2 + \kappa_-^2 - 2\kappa_+\kappa_-\cos(2\phi_0)], \tag{18}$$

where $A(\omega)$ is the spectral amplitude of the THz source, and J_1 is the Bessel function of the first order. The quantities $\kappa_\pm$ and β are given by

$$\kappa_\pm = \mathrm{sinc}\ \alpha_\pm, \tag{19}$$

$$\alpha_\pm = \frac{\pi L}{\lambda_{\mathrm{THz}}}\left(1 - \cos\Theta \pm \frac{\lambda_{\mathrm{THz}}}{2l_d}\right), \tag{20}$$

$$\beta = \frac{2\pi}{\lambda_{\mathrm{THz}}}a\sin\Theta, \tag{21}$$

with $\mathrm{sinc}(x) = \sin x/x$, and λ_{THz} denotes the wavelength associated with the THz frequency ω_{THz}. The functions $\kappa_\pm$, linked to the phase-matching condition for THz generation, depend on the extent (L) of the axial filament. The quantity β accounts for the radial dimensions of the plasma ($\beta \propto a$) entering the term $J_1^2(\beta)/\beta^2$ that describes the circular diffraction of the THz waves emitted by the plasma cylinder. For common filaments, the radius a is limited to a few tens of microns and $\Theta < 10^\circ$, i.e., $\beta \ll 1$ in the main part of the spectrum, so this diffraction term has limited influence. The maximum emission is reached for $\alpha_- = 0$, thus providing the theoretical emission angle Θ_p:

$$\cos\Theta_p = 1 - \frac{\lambda_{\mathrm{THz}}}{2l_d}. \tag{22}$$

The phase mismatch between the THz waves emitted at different places in the plasma filament causes destructive interference for the on-axis THz component for plasmas of length $L > l_d$, and the THz radiation propagates as a cone in space, far from the plasma volume. The emission angles are usually narrow, i.e., Θ is in the 2°–10° range [47,52,75,76].

As summarized in Fig. 1, the angular THz spectrum described by this model depends mainly on three parameters. The first parameter is the plasma length L. When $L < l_d$, the THz radiation is maximum on the optical axis ($\Theta = 0$), while for longer plasma lengths ($L > l_d$), the on-axis THz amplitude vanishes and the THz beam becomes a cone with angle Θ_p [see Fig. 1(a)]. The second key parameter is the electron density N_e. Figure 1(b) indicates that, at a fixed frequency, Θ_p increases for higher $N_e > 2 \times 10^{17}\ \mathrm{cm}^{-3}$, while it remains constant for lower density levels. The dephasing length l_d [Eq. (17)] decreases significantly as the value of N_e increases. For larger density levels, conical emission, therefore, appears for shorter plasma lengths. The third parameter is the radiated THz frequency ν. In this regard, Fig. 1(c) highlights that the emission angle Θ_p [Eq. (22)] strongly decreases with increasing ν (white curve), consistent with Eq. (18).

In addition to the above well-known properties, additional information can be extracted from the function describing the phase-matching condition in Eq. (18), namely,

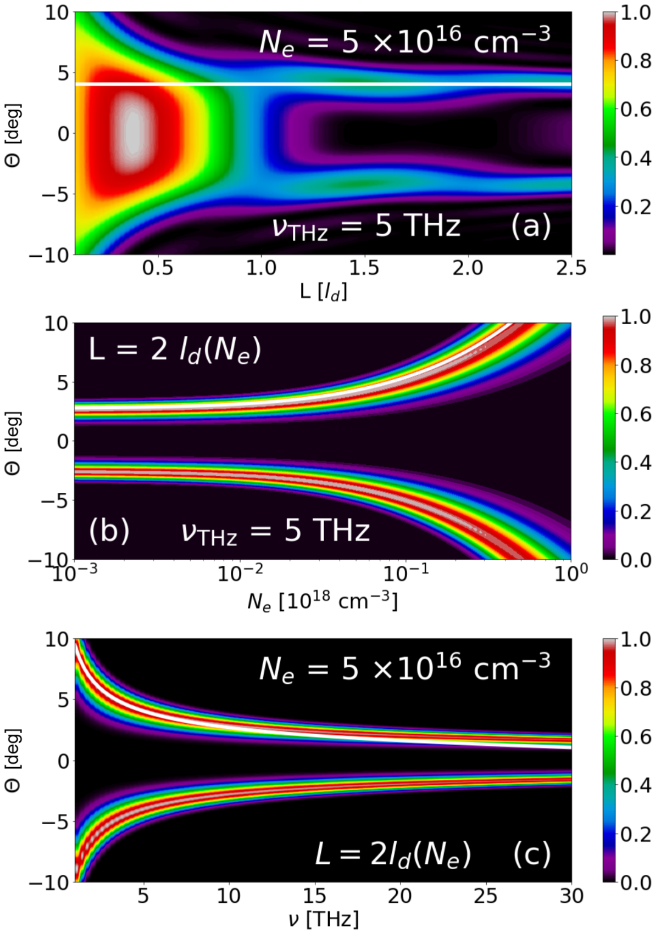

FIG. 1. Mapping of the angular terahertz (THz) spectral intensity $|\widehat{E}(\omega_{\rm THz},\Theta)|^2$ given by Eq. (18) as a function of the angle Θ and (a) the plasma length L, (b) the electron density N_e, and (c) the frequency $\nu=\omega_{\rm THz}/2\pi$. The maps are normalized to their respective maximum values, and we set $A(\omega)=1$ for simplicity (as in Ref. [48]). The white curves report the theoretical conical emission angle Θ_p predicted by Eq. (22).

$P(L,\Theta,\lambda_{\rm THz})\equiv L^2[\kappa_+^2+\kappa_-^2-2\kappa_+\kappa_-\cos(2\phi_0)]$. First, on-axis components associated with the interference function $P(L,\Theta{=}0,\lambda_{\rm THz}){=}(2l_d/\pi)^2[1-\cos(\pi L/l_d)][1-\cos(2\phi_0)]$ develop as a $2l_d$-periodic function of the plasma length L and reach maxima with constant amplitude at odd-numbered multiples of l_d, provided that the initial phase angle ϕ_0 differs from 0 [π]. Second, phase-matched off-axis components parabolically increase like $P(L,\Theta=\Theta_p,\lambda_{\rm THz})\simeq L^2[1+{\rm sinc}^2(\pi L/l_d)-2\cos(2\phi_0){\rm sinc}(\pi L/l_d)]$. They exceed the on-axis components from $L\approx l_d$ and increase monotonously to higher amplitude levels for longer plasma lengths. The value of ϕ_0 does not change this behavior and simply introduces secondary oscillations. Importantly, these properties result from interference in the far-field THz intensity spectrum.

In the following, we revisit this THz emission model by making it as general as possible. This includes (i) treating envelope effects, (ii) allowing for transverse variations in the plasma density, (iii) accounting for the characteristic spectral signatures of $A(\omega)$ that depend on the nonlinear propagation regime at play, and (iv) passing from LP-P to CP-S driver pulses.

B. THz conical emission: An augmented model

The electric field $\mathbf{E}(\mathbf{r},t)$ emitted by a conductive current density $\mathbf{J}(\mathbf{r},t)$ in a neutral plasma volume V reads [77]

$$\mathbf{E}(\mathbf{r},t)=-\frac{\mu_0}{4\pi}\int_V d^3\mathbf{r}'\frac{\partial_t\mathbf{J}(\mathbf{r}',t')}{|\mathbf{r}-\mathbf{r}'|},\tag{23}$$

where $t'=t-|\mathbf{r}-\mathbf{r}'|/c$ is the retarded time at which the signal is generated, and t is the time at which the detector receives the signal. We assume that the refractive index of the medium is $n_{\rm opt}(\omega_{\rm THz})\equiv 1$ in the THz frequency range. The notation $\mathbf{r}'$ applies to the local coordinates inside the plasma volume. Cartesian, cylindrical, and spherical coordinates are written as $(x,\ y,\ z)$, $(r,\ \varphi,\ z)$, and $(r,\ \Theta,\ \Phi)$, respectively. We are interested in the far-field distribution, so the distance between the plasma and the detector is large compared with the dimensions of the filament, that is, $|\mathbf{r}|\gg|\mathbf{r}'|$, which leads to the simplification of the Fourier-transformed field (see Appendix A):

$$\begin{aligned}&\widehat{\mathbf{E}}(r,\Theta,\Phi,\omega)\\&\quad=\frac{i\omega\mu_0}{4\pi r}\exp\left(i\frac{\omega}{c}r\right)\int_{-L/2}^{+L/2}dz'\exp\left(-i\frac{\omega}{c}\cos\Theta z'\right)\\&\qquad\times\iint d^2\mathbf{r}'_\perp\widehat{\mathbf{J}}(\mathbf{r}',\omega)\exp(-i\mathbf{k}_\perp\cdot\mathbf{r}'_\perp),\end{aligned}\tag{24}$$

with $\mathbf{k}_\perp=(\omega/c)(\sin\Theta\cos\Phi,\sin\Theta\sin\Phi)$. The double integral formally applies to the entire transverse plane. Here, $\widehat{\mathbf{J}}(\mathbf{r}',\omega)$ is zero for $|\mathbf{r}'|\to+\infty$, particularly when considering a finite plasma cylinder of radius a.

The second step consists of taking into account the Kerr polarization [Eq. (7)] through the substitution:

$$\mathbf{J}(\mathbf{r},t)\to\mathbf{J}_e(\mathbf{r},t)+\partial_t\mathbf{P}_K(\mathbf{r},t),\tag{25}$$

and calculating the free-electron contribution $\mathbf{J}_e(\mathbf{r},t)$ using, for technical convenience, a toy ionization rate satisfying $W(E)\propto E^2(t)$. This toy ionization rate, limited to single-photon ionization, was already employed in Refs. [60,78] and allows a semianalytical treatment that provides the major characteristics of multicolor-driven THz pulses, including their polarization state. Most importantly, it captures the asymmetries in the temporal location of the ionization peaks introduced by the second pump color, which are crucial for the photocurrent mechanism. In this respect, approaches based on Fourier series using more realistic, highly nonlinear ionization rates but involving only a single pump color [79,80] cannot account for these asymmetries.

The third step is to consider a pump field that admits transverse envelopes and different delays for the two pump colors. Introducing the retarded times $t'_{j=\{1,2\}}=t-z/v_{pj}$, with $v_{pj}=c/n(j\omega_0)$ being the respective phase velocities, our LP-P two-color laser field takes the general form:

$$\begin{aligned}\mathbf{E}_{\rm L}(\mathbf{r},t)&=\mathcal{E}_1(\mathbf{r},t'_1)\cos\left[\omega_0t'_1+\phi_1(\mathbf{r})\right]\mathbf{e_x}\\&\quad+\mathcal{E}_2(\mathbf{r},t'_2)\cos\left[2\omega_0t'_2+\phi_2(\mathbf{r})\right]\mathbf{e_x},\end{aligned}\tag{26}$$

where $\phi_j(\mathbf{r})$ is the spatial phase of the jth color. We assume that the envelopes $\mathcal{E}_j$ and the phases ϕ_j vary little along the filament, that is, they do not explicitly depend on z, and we can write $\mathcal{E}_j(\mathbf{r},t_1')\approx\mathcal{E}_j(\mathbf{r}_\perp,t_1')$ and $\phi_j(\mathbf{r})\approx\phi_j(\mathbf{r}_\perp)$. We note that this is a strong assumption, particularly for the phases, but necessary for the upcoming semianalytical treatment. In contrast, our UPPE simulation results comprehensively account for the complete spatiotemporal dynamics of the pump field. Furthermore, we assume that temporal and radial variations of the laser envelopes are separable as

$$\mathcal{E}_j(\mathbf{r}_\perp,t_j')=\mathcal{E}_{tr,j}(\mathbf{r}_\perp)\mathcal{E}_{ax,j}(t_j'),\tag{27}$$

where the maximum of $\mathcal{E}_{tr,j=1,2}$ is normalized to unity, and $\mathcal{E}_{ax,j}$ contains the electric field amplitude expressed in volts per meter.

Straightforward computations detailed in Appendix A then enable us to establish the following generic dependencies:

$$(\partial_t+\nu_c)\mathbf{J}_e^{\rm THz}(\mathbf{r},t)\propto\mathcal{E}_1^2(\mathbf{r}_\perp,t_1')\mathcal{E}_2(\mathbf{r}_\perp,t_2')\sin[\Delta kz+\phi(\mathbf{r}_\perp)]\mathbf{e_x},\tag{28}$$

$$\mathbf{P}_K^{\rm THz}(\mathbf{r},t)\propto\mathcal{E}_1^2(\mathbf{r}_\perp,t_1')\mathcal{E}_2(\mathbf{r}_\perp,t_2')\cos[\Delta kz+\phi(\mathbf{r}_\perp)]\mathbf{e_x},\tag{29}$$

where Δk is the phase mismatch in wave number between the harmonics and $\phi(\mathbf{r}_\perp)$ their phase angle:

$$\Delta k=\frac{2\omega_0}{c}[n(\omega_0)-n(2\omega_0)]=\pi/l_d,\tag{30}$$

$$\phi(\mathbf{r}_\perp)\equiv\phi_2(\mathbf{r}_\perp)-2\phi_1(\mathbf{r}_\perp).\tag{31}$$

Further computations lead to

$$|\widehat{\mathbf{E}}(\mathbf{r},\omega)|^2=\frac{\mu_0^2}{16\pi^2r^2}|\mathbf{C}_J(\Theta,\Phi,\omega)+\mathbf{C}_K(\Theta,\Phi,\omega)|^2,\tag{32}$$

where the functions $\mathbf{C}_J(\Theta,\Phi,\omega)$ and $\mathbf{C}_K(\Theta,\Phi,\omega)$ represent the contributions to the THz yield from the photocurrents (index J) and the Kerr effect (index K), respectively. These general functions are expressed as

$$\mathbf{C}_{J,K}(\Theta,\Phi,\omega)=A_{J,K}(\omega)\mathbf{I}_{J,K}(\Theta,\Phi,\omega),\tag{33}$$

with $A_{J,K}(\omega)$ containing the frequency dependency of the considered source term and $\mathbf{I}_{J,K}(\Theta,\Phi,\omega)$ being the associated angle-dependent longitudinal phase matching function, namely,

$$\mathbf{I}_J^{\text{LP-P}}(\Theta,\Phi,\omega)=\frac{L}{2}[I_S^+\kappa_+-I_S^-\kappa_-]\mathbf{e_x},\tag{34}$$

$$\mathbf{I}_K^{\text{LP-P}}(\Theta,\Phi,\omega)=i\frac{L}{2}[I_S^+\kappa_++I_S^-\kappa_-]\mathbf{e_x}.\tag{35}$$

Here, $\kappa_\pm$ are those given in Eq. (19).

The quantities $I_S^\pm$ describe the transverse effects of the emitting source on the far-field THz radiation:

$$I_S^\pm(\Theta,\Phi,\omega)=\mathcal{F}_\perp\{J_{\rm tr}(\mathbf{r}_\perp)\exp[\pm i\phi(\mathbf{r}_\perp)]\}(\Theta,\Phi,\omega),\tag{36}$$

where notation $\mathcal{F}_\perp$ refers to the Fourier transform with respect to the transverse variables $\mathbf{r}_\perp$, and

$$J_{\rm tr}(\mathbf{r}_\perp)=\mathcal{E}_{{\rm tr},1}^2(\mathbf{r}_\perp)\mathcal{E}_{{\rm tr},2}(\mathbf{r}_\perp)\tag{37}$$

represents the transverse envelope of the source terms. Here, I_S reduces to the Bessel-like circular diffraction function recalled in Eq. (18) for a cylindrical homogeneous plasma of radius a (see Appendix B). We also mention that CP-S pulses can be treated similarly, cf. Appendix A, and one finds

$$\mathbf{I}_J^{\text{CP-S}}(\Theta,\Phi,\omega)=\frac{L}{2}\begin{pmatrix}I_S^+\kappa_+-I_S^-\kappa_-\\ I_S^+\kappa_++I_S^-\kappa_-\end{pmatrix},\tag{38}$$

$$\mathbf{I}_K^{\text{CP-S}}(\Theta,\Phi,\omega)=i\frac{L}{2}\begin{pmatrix}I_S^+\kappa_++I_S^-\kappa_-\\ -I_S^+\kappa_++I_S^-\kappa_-\end{pmatrix}.\tag{39}$$

By construction, our model does not account for variations in the plasma density along z, and plasma absorption and opacity are also neglected for reasons addressed in Appendix A.

Integration of our model requires some prior knowledge of key parameters of the emitting filament. First, we need to model the transverse shape of the THz source $J_{\rm tr}(\mathbf{r}_\perp)$ to calculate $I_S^\pm$. To this end, we use our linear laser propagation code up to a point $z=z_p$, where the width of the laser beam is small enough to reach high intensities corresponding to efficient plasma generation. At this distance, assuming that the envelopes of the two colors remain superimposed in time, we can extract the quantities $\phi(\mathbf{r}_\perp)$ and the transverse field profiles, allowing us to reconstruct $J_{\rm tr}(\mathbf{r}_\perp)$ at this distance and thus evaluate $I_S^\pm$. Second, as addressed in Appendix A for illustrative purposes, Gaussian temporal envelopes impose a radiated Gaussian spectrum. This is unrealistic because the temporal pump pulse profiles strongly evolve along propagation due to the Kerr and plasma response, and the THz spectra obtained from experiments or simulations look very different. We therefore replace the profiles $A_{J,K}(\omega=2\pi\nu)$ in Eq. (33) by typical spectral shapes delivered by the respective source term in the specific propagation regime under consideration. In what follows, we use

$$A_J(\nu)\propto\left[1-\exp\left(-\frac{\nu}{f_{\max}}\right)\right]\exp\left[-\left(\frac{\nu}{f_0}\right)^2\right],\tag{40}$$

$$A_K(\nu)\propto\left[1-\exp\left(-\frac{\nu}{f_{\max}}\right)\right]\exp\left[-\left(\frac{\nu}{f_0}\right)^4\right],\tag{41}$$

yielding the synthetic profiles shown in Fig. 2 for typical THz spectra produced by photocurrents alone (blue curve), or the Kerr effect discarding SRRS (red curve) in short-range focused (solid) or long-range filamentation (dashed curves) regimes, both illustrated in the top insets of Fig. 2. They have been inspired by Figs. 3(c) and 3(d) of Ref. [64] and Fig. 2 of Ref. [63] and are comparable with our transversely integrated UPPE spectra (not shown). Typically, in the focused regime, plasma-driven (photocurrents) THz spectra go up to ~70–100 THz, while the bound electron (Kerr) response only produces THz waves below ~40 THz. In the long-range filamentation regime, nonlinearities develop a supercontinuum through which the THz spectrum can even merge with the broadened optical pump spectrum [81]. The Kerr contribution to the THz spectrum may be extended to 80 THz. Three typical situations will be explored in the following three subsections: purely plasma-driven emission in the focused regime, photocurrents interplaying with a strong Kerr response in the focused regime, and the long-range filamentation regime accounting for both plasma-driven and Kerr THz contributions.

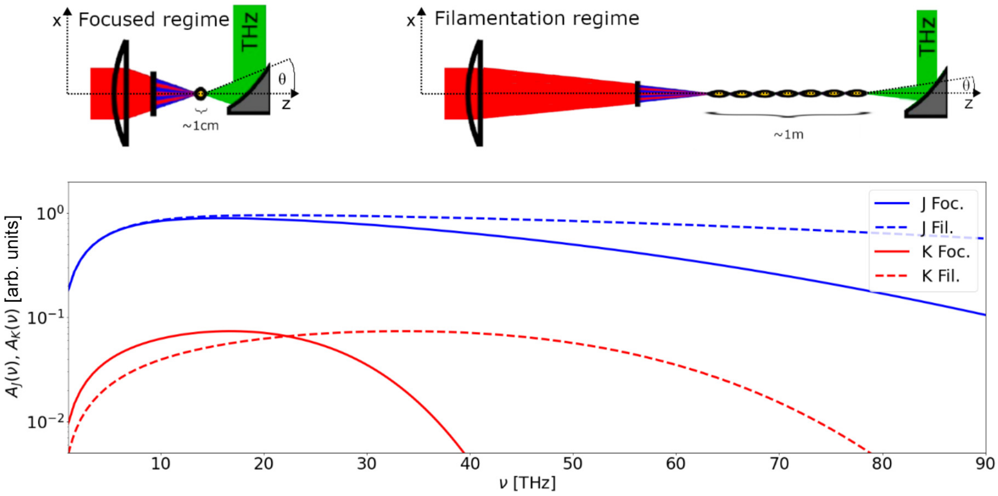

FIG. 2. Top: Insets recall the two baseline propagation regimes studied here, namely, the focused propagation geometry (left) characterized by a short, cm-long interaction plasma zone and broadband THz spectra and the long-range filamentation geometry (right) characterized by extended, meter-range plasma channels and ultrabroadband THz spectra. Bottom: Characteristic shapes of THz spectra due to photocurrents (blue curves) and Kerr effect (red curve) in focused (solid curves) and filamentation (dotted curves) regimes inspired from Refs. [63,64]. The fraction of the Kerr response can increase up to 10% in amplitude in the filamentation regime or up to 77% in the strong Kerr regime. Parameters in Eq. (40) are $f_{\max} = 5\,\text{THz}$ and $f_0 = 60\,\text{THz}$ in the focused regime and $f_{\max} = 5\,\text{THz}$ and $f_0 = 120\,\text{THz}$ in the filamentation regime. Parameters in Eq. (41) are $f_{\max} = 10\,\text{THz}$ and $f_0 = 30\,\text{THz}$ in the focused regime and $f_{\max} = 5\,\text{THz}$ and $f_0 = 60\,\text{THz}$ in the filamentation regime.

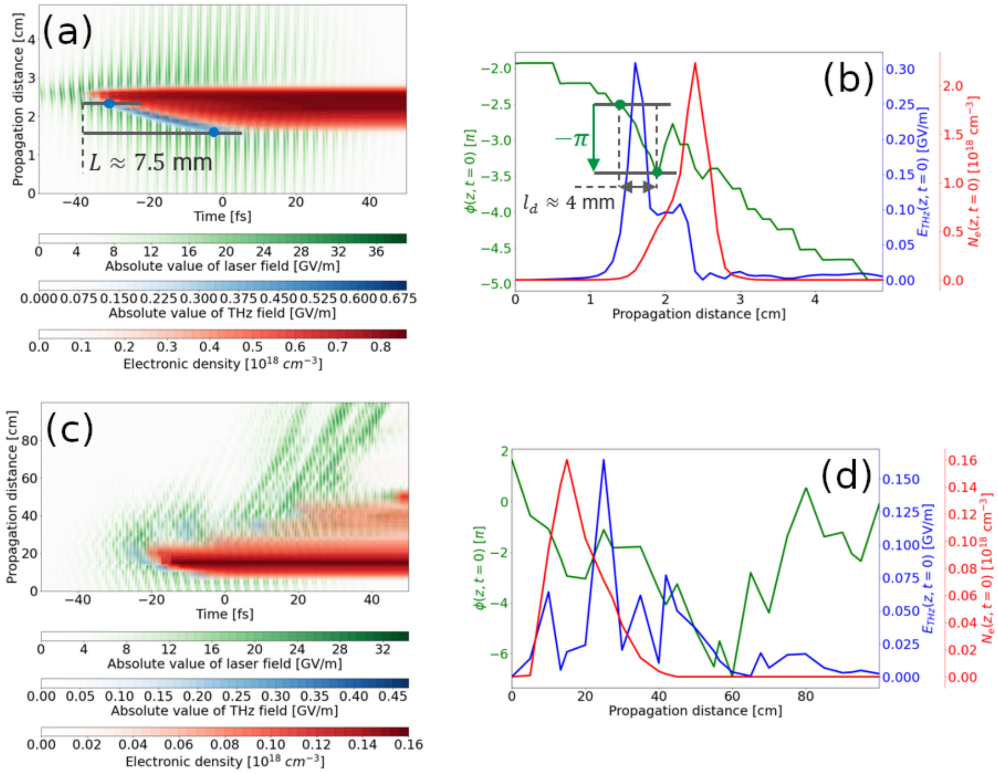

FIG. 3. Left-hand side column: On-axis terahertz fields (blue areas) generated by two-color laser fields (green curves) that trigger electron plasma densities (red areas) in the (z, t) plane in (a) the focused regime and (c) the filamentation regime. Right-hand side column, (b) and (d): Corresponding on-axis relative phase between the fundamental and second harmonic $\phi(z, t) = \phi_2(z, t) - 2\phi_1(z, t)$ at $t = 0$ together with the created THz field and plasma density. The simulation parameters are detailed in the respective subsections below.

Lastly, the "conical" functions $\kappa_\pm$ are obtained by estimating the plasma length L and the on-axis electron density N_e, which provides the dephasing length l_d. In estimating N_e, one has to remember that the THz waves are produced before the air plasma is fully established [75], which means that the peak electron density (henceforth denoted by $N_e^{\max}$) is considerably higher than the effective electron density N_e^{eff} that should be used in the model. Illustrative examples obtained from UPPE simulations are given in Fig. 3, detailing the maps of THz fields emerging from the interaction between the two-color laser field and the generated free electron density created in focused or filamentation regimes. We can observe that in the focused regime [Figs. 3(a) and 3(b)] the THz field is always created at the front of the plasma, which justifies that the effective density level N_e^{eff} associated with the emitted THz wave is always lower than the peak plasma density. Another important observation is that the effective plasma length L corresponding to the longitudinal distance over which the THz field is emitted remains approximately on the order of the distance over which the relative phase between the two laser harmonics undergoes a π phase shift, that is, $L \gtrsim l_d$. By contrast, in the filamentation regime [Figs. 3(c) and 3(d)], we can see that, although the THz pulse still emerges at the plasma front along Kerr self-focusing–plasma-defocusing sequences, the plasma length generally satisfies $L \geqslant 2\, l_d$.

C. Focused regime without Kerr response

In this subsection, we compare the results of our augmented model with the predictions of You *et al.* [48] and confront them with UPPE simulation results. We simulate the nonlinear propagation of a two-color LP-P Gaussian laser pulse with 0.8 μm fundamental wavelength, 500 μJ energy, 34 fs duration, and 250 μm initial radius. Here, 35% of the laser energy is allocated to the second harmonic with zero relative phase. First, the pulse is focused in air by a lens of 2.6 cm focal length. The ionization is modeled with the PPT rate [62] ($Z^*_{\text{O}_2} = 0.53$, $Z^*_{\text{N}_2} = 0.9$). To make photocurrents the only source of THz radiation in the simulation, we neglect the Kerr response and SRRS by setting the nonlinear index of air n_2 to zero.

Figures 4(a) and 4(b) plot the evolutions of the maximum electron density along z and the THz energy contained in the simulation window, with the associated effective density N_e^{eff} at the time instants when the THz field is maximum. The peak density $N_e^{\max}$ is rather constant $\approx 10^{18}\,\text{cm}^{-3}$ (respectively, $N_e^{\text{eff}} \approx 2 \times 10^{17}\,\text{cm}^{-3}$) during the increase in THz energy, taking place between 1.5 and 2.25 cm. Figures 4(c)–4(e) illustrate the angular THz intensity spectra calculated by Fourier transform in time and transverse space at $z = 1.75$ cm (plasma onset), $z = 2$ cm (middle), and $z = 2.5$ cm (end of the emitting zone). Upon laser propagation, the initial on-axis THz radiation progressively transforms into a cone, starting from the upper part of the spectrum. This spectral pattern is often met in the literature [47,75]. The generic coexistence of on-axis emission at low frequencies with a donut-shaped emission at large THz frequencies in such focused propagation regimes [47,53] is associated with an effective plasma length L that remains close to the dephasing length l_d, as justified by Figs. 3(a) and 3(b). The spectrum plotted in Fig. 4(e) contains all the THz energy produced during the simulation. It presents a notable contribution on the optical axis for $\nu < 10$–15 THz, and conical emission at $\Theta \approx 3°$ for $\nu > 15$ THz.

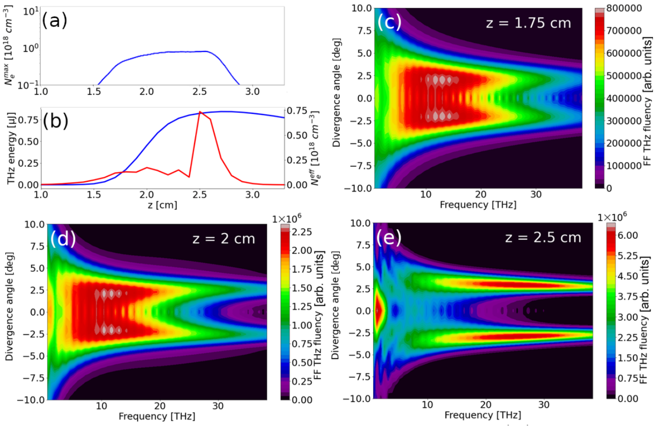

FIG. 4. Results of unidirectional pulse propagation equation (UPPE) simulations for laser-air parameters described in the text. Evolutions along z of (a) maximum electron density and (b) THz energy ($\nu < 90$ THz) in the simulation box (blue curve, left axis) and plasma density at the instants when the THz field is maximum (red curve, right axis). (c)–(e) Angular THz spectra in intensity calculated by transverse Fourier transform of the THz field at three different propagation distances.

We now compare Figs. 4(c)–4(e) with the angular intensity spectra predicted by the model of You *et al.* [48] and by our augmented model in Fig. 5. We assume that the only source of THz waves is photocurrents [$A_{\text{K}}(\omega) = 0$]. Because we operate in the focused regime, the spectrum $A_J(\omega)$ is taken as the solid

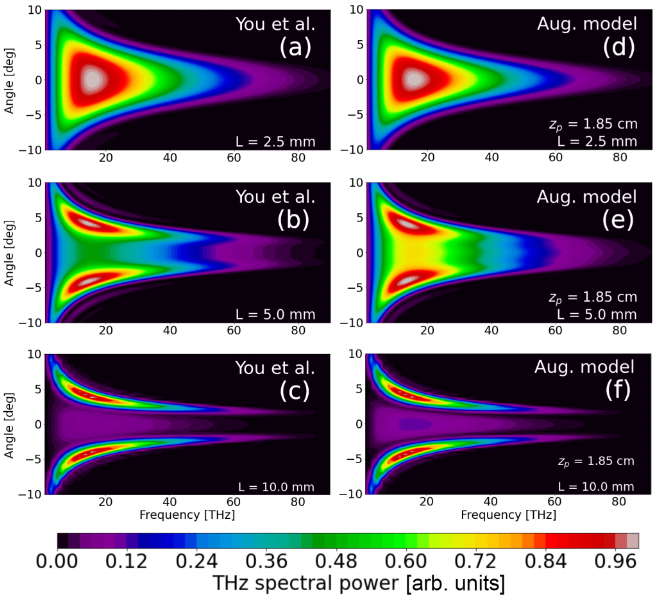

FIG. 5. THz angular spectra evaluated by (a)–(c) the model of You *et al.* [48] and (d)–(f) our augmented model at (a) and (d) $z = 1.75$ cm ($L = 2.5$ mm), (b) and (e) $z = 2$ cm ($L = 5$ mm), and (c) and (f) $z = 2.5$ cm ($L = 10$ mm). The laser-gas parameters are specified in the text; $z_p = 1.85$ cm.

blue curve of Fig. 2. When integrating the model of You *et al.* [48], the plasma radius is chosen as $a = 30\,\mu\text{m}$, and the effective electron density is $N_e^{\text{eff}} = 2 \times 10^{17}\,\text{cm}^{-3}$, yielding the dephasing length $l_d = 4\,\text{mm}$. The maximum emitter length is determined by the growth of THz energy, thus $L = 0.75\,\text{cm}$, as justified above. When integrating our augmented model, we employ the same input laser-air parameters in our linear propagator as those used in the UPPE simulation. The relative phase $\phi_0 = \pi/4$ between the two colors is chosen at the input ($z = 0$). We propagate the laser pulse linearly up to $z_p = 1.85\,\text{cm}$ ($f = 2.6\,\text{cm}$), where the laser fluency takes a shape like that calculated by UPPE, i.e., it reaches a transverse Gaussian profile being $75\,\mu\text{m}$ wide (not shown). The corresponding laser amplitude was checked to provide the same peak plasma density value ($N_e^{\max} \approx 10^{18}\,\text{cm}^{-3}$) as in Fig. 4(a), and a $50\,\mu\text{m}$ wide transverse plasma density profile.

Figure 5 illustrates the results given by (a)–(c) the model of You *et al.* [48] and (d)–(f) our augmented model at $z = 1.75$, 2, and 2.5 cm. At these distances, the effective plasma length L is 2.5, 5, and 10 mm, respectively. We notice that the spectra predicted by the two models in the cases where $L < l_d$ [Figs. 5(a) and 5(d)] and $L > l_d$ [Figs. 5(c) and 5(f)] are very similar, confirming that the model of You *et al.* [48] is well suited for radially symmetric plasma channels. When $L = 5\,\text{mm} \approx l_d$, both models qualitatively reproduce the on-axis contribution predicted by the UPPE simulation. However, this on-axis component is stronger in the augmented model and is therefore better represented quantitatively by this model [Fig. 5(e) to be compared with Fig. 5(b)]. This difference comes from the phase modulation caused by the phase term $\exp[\pm i\phi(\mathbf{r}_\perp)]$ in Eq. (36), which accounts for additional interferences between the THz waves formed in the overall plasma volume. This effect is absent in the model of You *et al.* [48]. Note that, for $L = 10\,\text{mm} \approx 3\,l_d$, revivals of on-axis emission occur in this spectral dynamics—in agreement with the interference function $P(L, 0, \lambda_{\text{THz}})$ discussed in the previous subsection—and they are more pronounced in the augmented model.

D. Focused regime with strong Kerr response

We now examine what happens when a relevant Kerr contribution affects the former focused propagation. A second UPPE simulation was carried out with a strong instantaneous Kerr polarization by setting $x_K = 0$ and $n_2 = 3.8 \times 10^{-19}\,\text{cm}^2/\text{W}$. This choice of x_K implies that SRRS is ignored, which maximizes self-focusing and related four-wave mixing.

Figure 6(a) shows that the maximum plasma density value, $N_e^{\max} \approx 10^{19}\,\text{cm}^{-3}$, is ~10 times higher than in the previous configuration, which is caused by the strong Kerr self-focusing effect. Noticeably, this increase in density does not induce a growth in the laser-to-THz conversion efficiency [compare Figs. 4(b) and 6(b)]. The THz energy in the simulation box increases between 1.5 and 2.5 cm, hence $L = 10\,\text{mm}$. Although the density strongly varies with z, we select $N_e^{\text{eff}} \approx 3 \times 10^{17}\,\text{cm}^{-3}$ [consistent with the red curve in Fig. 6(b)], which corresponds to a dephasing length $l_d = 2.8\,\text{mm}$. Figures 6(c)–6(e) illustrate the angular THz spectra calculated by the UPPE code at $z = 1.75$, 2, and 2.5 cm. Again, the corresponding plasma lengths L are 2.5, 5, and 10 mm. These spectra present strong on-axis components whose amplitudes increase along propagation. On-axis emission occurs in the frequency range 10–25 THz, which we attribute to the strong Kerr self-focusing that affects the pump pulse propagation dynamics [64]. Photocurrent-induced off-axis emission ($\Theta = 3^\circ$–4°) fully develops for high frequencies $\nu > 20\,\text{THz}$ in Figs. 6(d) and 6(e), where the criterion $L > l_d$ is fulfilled.

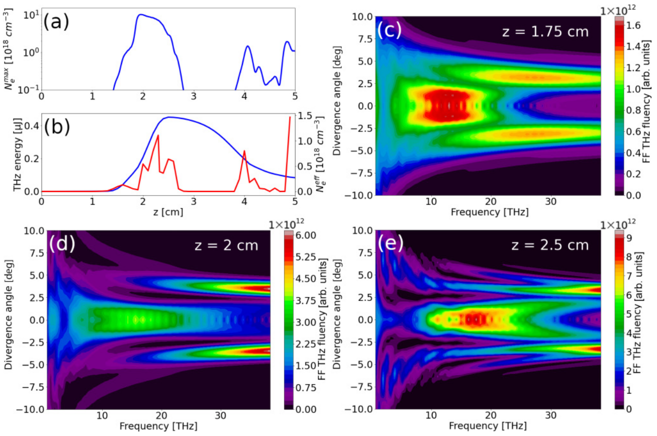

FIG. 6. UPPE results displaying the same quantities as in Fig. 4 for a medium with strong Kerr response ($x_K = 0$, $n_2 = 3.8 \times 10^{-19}\,\text{cm}^2/\text{W}$).

Now let us evaluate the THz radiation using our semi-analytical model. The functions $A_J(\omega)$ and $A_K(\omega)$ are taken as the solid blue and $\mathbf{r}_\perp$ red curves of Fig. 2, respectively, with the Kerr maximum spectral amplitude being 77% of the photocurrent one. Here, we linearly propagated the laser pulse up to $z_p = 2\,\text{cm}$ (instead of $z_p = 1.85\,\text{cm}$) because stronger Kerr self-focusing fosters a more narrow plasma channel whose equivalent diameter is attained at longer distances z upon linear propagation. The amplitude of the optical field reached at $z = z_p$ then corresponds to a peak electron density of $10^{19}\,\text{cm}^{-3}$, in agreement with Fig. 6(a).

Figure 7 shows the results of (a) and (b) the model of You *et al.* [48] and (c)–(f) the augmented model for the same plasma lengths as analyzed in Fig. 6, completed with additional information for $L = 8\,\text{mm}$. The two models predict similar conical emission angles. However, the angular spectra predicted by our augmented model include an extra contribution on the optical axis, peaked around $\nu = 15\,\text{THz}$, which is shaped by the spectral amplitude $|A_J(\omega) - i\omega A_K(\omega)|$, where the parabolic Kerr contribution, here artificially increased, is absent in the model of You *et al.* [48]. In the full plasma regime ($z \approx 2.3\,\text{cm}$), Figs. 7(b) and 7(e) both describe a net conical emission due to photocurrents at angles between 3° and 5°, yet only the augmented model produces off-axis emissions ($\Theta \lesssim 3.5^\circ$) that develop in the high-frequency range $>25\,\text{THz}$, like the UPPE simulations. On-axis revivals are more pronounced for $L = 8\,\text{mm} \simeq 3\,l_d$ in the augmented model and reach a maximum at $\nu \approx 15\,\text{THz}$, due to our parabolic spectral profile. Radial phase variations $\phi(\mathbf{r}_\perp)$ are also expected to contribute on-axis, following Figs. 5(e) and 5(f) of the previous subsection. The difference with UPPE data may be explained by the strong nonlinearities producing

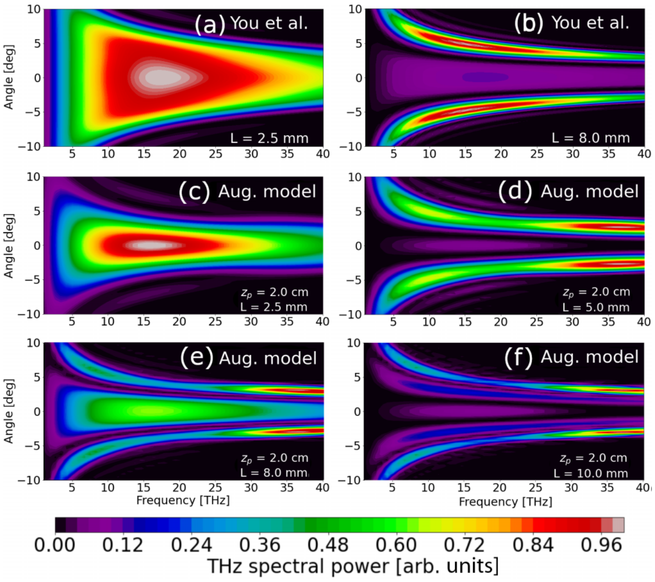

FIG. 7. Angular THz spectra evaluated by (a) and (b) the model of You *et al.* [48] and (c)–(f) our augmented model at (a) and (c) $z = 1.75$ cm ($L = 2.5$ mm), (d) $z = 2$ cm ($L = 5$ mm), (b) and (e) $z = 2.3$ cm ($L = 8$ mm), and (f) $z = 2.5$ cm ($L = 10$ mm); $z_p = 2$ cm. See text for details.

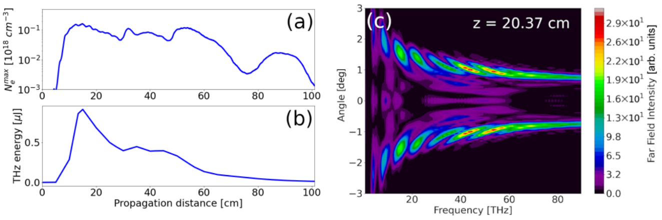

FIG. 8. (a) Maximum electron density and (b) THz energy ($\nu < 90$ THz) contained in the UPPE simulation window as a function of z for a two-color long-range filament. (c) Angular THz spectrum calculated at $z \simeq 20.4$ cm.

Kerr self-modulation and plasma defocusing, which render the plasma density in the UPPE simulation inhomogeneous, hence contradicting the model assumptions. On-axis components decrease to lower amplitudes in the semianalytical spectra, whereas they increase along z in the UPPE simulation data. Finally, we underline that the angular spectra computed from the augmented model become closer to the patterns of You *et al.* [48] when the Kerr spectral amplitude decreases below 50% of the photocurrent spectral amplitude. This indicates that such large on-axis components developed in the UPPE simulations cannot be caused directly by the Kerr response alone.

E. Filamentation regime

We conclude this section by addressing the long-range filamentation regime. Here, the UPPE code was used to simulate a two-color laser pulse ($r = 35\%$) with fundamental operating at 0.8 μm, duration of 34 fs, initial radius of 2.5 mm, and energy of 1.5 mJ, loosely focused in the air (20% O_2, 80% N_2; $n_2 = 3.8 \times 10^{-19}$ cm^2/W, $x_K = 0.8$) by a lens of focal length $f = 2.6$ m. For such a beam, using the linear preprocessor was necessary to perform a linear propagation of the laser pulse over 2.3 m until reaching intensities close to the Kerr nonlinearity threshold. The resulting pulse was then used as the input condition for the UPPE code at $z = 0$.

No multiple filamentation occurs (not shown), as the input peak power remains rather close to critical $P_{\rm cr}$ [82], i.e., $P_{\rm in} \simeq 2.6\,P_{\rm cr}^{\rm inst}$, where $P_{cr}^{\rm inst} \equiv P_{cr}/(1 - x_k)$ refers to the instantaneous critical power. Figure 8(a) shows that the extended filament maintains a relatively constant maximum electron density $\approx 10^{17}$ cm^{-3} between $z = 10$ and 60 cm, due to clamping effect, then turns off afterward. Figure 8(b), plotting the THz energy in the simulation box along z, shows a strong decrease beyond $z = 18$ cm, due to the THz radiation leaving the simulation box. Moreover, THz field production becomes less efficient at such long distances because the temporal overlap between the two laser harmonics deteriorates through temporal walk-off. Figure 8(c) describes the THz spectrum calculated at $z \simeq 20.4$ cm. We can evaluate from Figs. 3(c), 8(a), and 8(b) a minimum length $L_{\rm min} \simeq 5$ cm associated with an efficient plasma emitting zone in this configuration. This length corresponds to the distance that a THz wave generated on-axis ($x = y = 0$) at an angle $\Theta \approx 1.5°$ must travel to leave the simulation box with a transverse window extending from −1.3 to 1.3 mm.

Setting $L = 5$ cm, the effective electron density can be estimated as $N_e^{\rm eff} \approx 10^{16}$ cm^{-3} from Figs. 8(a) and 8(b). Note that, for such density levels, the dephasing length depends little on $N_e^{\rm eff}$, so that 2 cm $\leqslant l_d <$ 2.6 cm $< L$. We linearly propagated the same laser pulse over a distance of $z_p =$ 2.6 m to integrate our augmented model. We chose $A(\omega)$ and $A_{J,K}(\omega)$ as given by Fig. 2 (dashed curves), where the Kerr component is ∼10% that of photocurrents in intensity. Figures 9(a) and 9(b) plot the angular spectra calculated from the model of You *et al.* [48] and ours, respectively. These spectra are almost identical: They present a conical emission for $\Theta = 1$–$2°$ with a flat frequency profile, which agrees with the UPPE simulation. The residual central emission (<10% in spectral power) is consistent with the expected on-axis contribution for $L < 2\,l_d$.

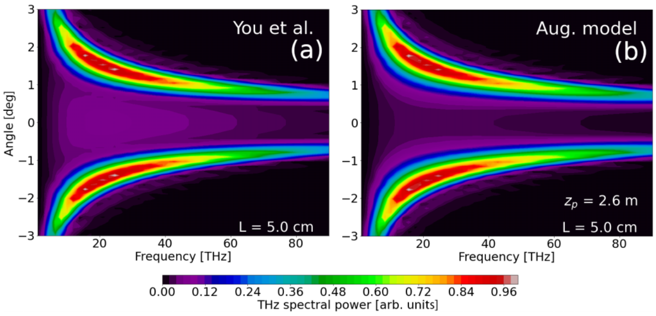

FIG. 9. Angular THz spectra estimated using (a) the model of You *et al.* [48] and (b) our augmented model for the filamentation setup. Laser-medium parameters are specified in the text.

IV. INFLUENCE OF OPTICAL ABERRATIONS

In this section, we aim to characterize the impact of common OAs on the nonlinear propagation of two-color pulses producing THz radiation. OAs modify the propagation of a laser beam through distortion of its transverse phase, thus of its optical wavefront [83]. They tend to alter the position and shape of the focal spot and, thereby, the geometry of the plasma channel. OAs are usually classified using two integers: the radial degree n and the azimuthal degree $m \leqslant n$ entering the Zernike polynomial $Z_n^m(\rho, \Phi)$ [58]:

$$Z_n^m(\rho, \Phi) = \begin{cases} R_n^m(\rho)\cos(m\Phi) & \text{if } m \geqslant 0 \\ -R_n^{-m}(\rho)\sin(m\Phi) & \text{if } m < 0 \end{cases}, \tag{42}$$

where $\rho \equiv \sqrt{2}r_\perp/w_0$, with $r_\perp = \sqrt{x^2+y^2}$ and w_0 being the beam width. Here,

$$R_n^m(\rho) = \sum_{k=0}^{\frac{n-m}{2}} \frac{(-1)^k(n-k)!}{k!\left(\frac{n+m}{2}-k\right)!\left(\frac{n-m}{2}-k\right)!}\rho^{n-2k} \tag{43}$$

is the radial distribution for $n-m$ even, and $R_n^m(\rho) \equiv 0$ otherwise.

Below, we shall concentrate on the basic configuration of focus ($n=2$, $m=0$)—consisting of a simple focusing lens effect—and will add to this elementary lensing three characteristic OAs of interest, namely, vertical astigmatism ($n=m=2$), vertical coma aberration ($n=3$, $m=-1$), and sphericity ($n=4$, $m=0$). For these four configurations, the polynomials $Z_n^m(\rho, \Phi)$ express as

$$\text{Focus} \qquad Z_2^0(\rho) = 2\rho^2 - 1, \tag{44}$$

$$\text{Astigmatism} \qquad Z_2^2(\rho, \Phi) = \rho^2\cos(2\Phi), \tag{45}$$

$$\text{Coma} \qquad Z_3^{-1}(\rho, \Phi) = (3\rho^3 - 2\rho)\sin(\Phi), \tag{46}$$

$$\text{Sphericity} \qquad Z_4^0(\rho) = 6\rho^4 - 6\rho^2 + 1. \tag{47}$$

Each OA is associated with an amplitude coefficient c_n^m, which has the dimension of a distance and determines the impact of the respective OA on the transverse phase of the beam. The total phase distortion is then conveniently expressed as

$$-\frac{\omega}{c}Z_{\text{OA}}(r_\perp, \Phi) = -\frac{\omega}{c}\sum_{n,m\leqslant n} c_n^m Z_n^m\left(\frac{\sqrt{2}r_\perp}{w_0}, \Phi\right). \tag{48}$$

The polynomial $Z_{\text{OA}}(r_\perp, \Phi)$ henceforth substitutes the transverse spatial dependency of the phase term $r_\perp^2/2f$ in Eq. (4). The sum symbol means that, when considering OAs such as sphericity, astigmatism, or coma, we add the latter to the baseline focus configuration.

Figure 10(a) depicts linear laser propagation in the absence of OA (i.e., with focus only). The initially 250 μm wide optical pulse is focused in air by a lens with focal length $f = 2.6$ cm. The inset shows the initial spatial phase of the laser pulse, corresponding to the Zernike polynomial $Z_2^0(r_\perp)$ linked to the focusing effect. This reference case is compared with sphericity ($c_4^0 = 5$ nm), astigmatism ($c_2^2 = 300$ nm), and coma ($c_3^{-1} = 300$ nm), further added to focus.

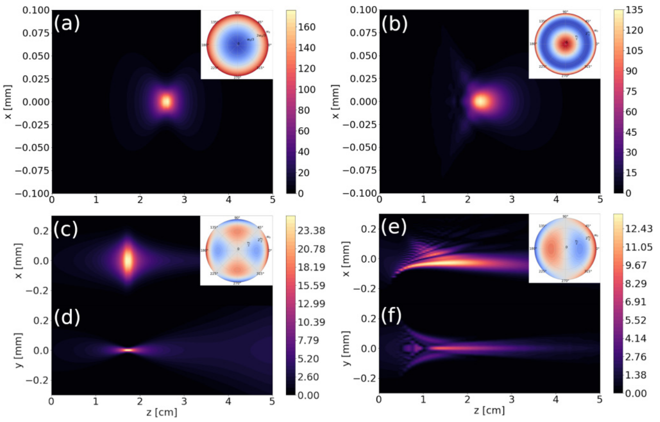

FIG. 10. Laser fluency maps in the linear regime (a–c) and (e) in the (x, z) plane and (d) and (f) in the (y, z) plane for a two-color laser pulse with 800 nm fundamental ($r = 35\%$) and initial radius $w_0 = 250$ μm focused in the air by a lens of focal length $f = 2.6$ cm (a) without additional optical aberration and with added (b) sphericity ($c_4^0 = 5$ nm), (c) and (d) astigmatism ($c_2^2 = 300$ nm), and (e) and (f) coma ($c_3^{-1} = 300$ nm). Insets show the corresponding laser spatial phases at $z = 0$.

Figures 10(b)–10(f) evidence that laser propagation is strongly influenced by the OAs. Astigmatism and coma introduce transverse asymmetries. In the following, we discuss nonlinear UPPE simulation results characterizing the impact of astigmatism, coma, and sphericity in the focused regime. We begin by addressing LP-P laser fields, which we will compare to circularly polarized beam (CP-S) simulations. Finally, we present results in the filamentation regime for OA-influenced LP-P laser pulses. UPPE far-field spectra are compared with the results of our augmented model.

A. LP-P polarization

Our two-color laser driver again involves a 0.8 μm fundamental pulse with 34 fs duration and 250 μm initial radius. The laser energy is 500 μJ, with $r = 35\%$ in the second harmonic; the pump beam is linearly polarized (LP-P) along $\mathbf{e_x}$ and focused ($f = 2.6$ cm equivalent to $c_2^0 = 300$ nm) in air ($n_2 = 3.8 \times 10^{-19}$ cm^2/W, $x_k = 0.8$) to provide us with the reference case (focus). We then carried out three other simulations including sphericity ($c_4^0 = 5$ nm), astigmatism ($c_2^2 = 300$ nm), and coma ($c_3^{-1} = 300$ nm) imposed at $z = 0$.

To start with, Fig. 11 shows the evolution of the laser fluencies calculated with the UPPE code in the nonlinear regime. The propagation dynamics look like those observed in the linear regime (compare with Fig. 10). Differences (reduction) in the maximum fluency values can be attributed to the clamping of the maximum laser intensity by the peak plasma density, as indicated by the blue isocontour density levels $N_e^{\max} = 5 \times 10^{16}$ cm^{-3}. For the reference case [Fig. 11(a)] and in the presence of sphericity [Fig. 11(b)], the plasma remains axisymmetric. However, adding astigmatism [Figs. 11(c) and 11(d)] and coma [Figs. 11(e) and 11(f)] breaks the transverse symmetry. Note that, in the configuration with coma, the plasma is, in fact, composed of a filament extending along the laser propagation direction, accompanied by small off-axis zones with nonzero electron density around $z = 1$ cm.

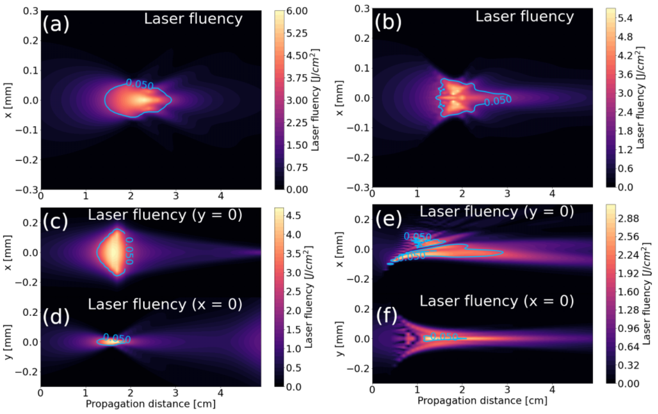

FIG. 11. UPPE-computed maps of the laser fluency for a two-color linear polarization–parallel (LP-P) pulse propagating in nonlinear regime (a–c) and (e) in the (x, z) plane and (d) and (f) (y, z) plane (a) in the reference (focus) case, with added (b) sphericity, (c) and (d) astigmatism, and (e) and (f) coma aberration. The blue lines show density isocontours at $N_e^{\max} = 5 \times 10^{16}\,\mathrm{cm}^{-3}$. Simulation parameters are specified in the text.

Figure 12(a) describes the axial evolutions of the maximum electron density for the four considered configurations. Compared with focus (reference case, blue curve), reaching a peak electron density of $N_e^{\max} \approx 2\text{–}3 \times 10^{18}\,\mathrm{cm}^{-3}$, astigmatism (green curve) and coma aberration (magenta curve) reach lower density levels by a factor of ≈ 2 and ≈ 5, respectively. Sphericity generates very intense density peaks ($N_e \approx 10^{19}\,\mathrm{cm}^{-3}$) corresponding to the off-axis hot spots visible in the laser fluence map of Fig. 11(b) at $z \simeq 1.8\text{–}2$ m. Sphericity produces a longer plasma channel than is observed in the focus case, which is in accordance with Refs. [84,85]. Astigmatism leads to a shorter plasma because this aberration induces an additional focusing effect. Coma generates a longer and smoother plasma channel because it decreases the maximum fluency level (and, therefore, the peak electron density). Plasma generation starts at smaller z distances, in accordance with Figs. 10(e) and 10(f). Figure 12(b), plotting the THz energy ($\nu < 90\,\mathrm{THz}$) accumulated along z in the simulation window, shows that OA hardly modifies the laser-to-THz conversion efficiency, except for coma, for which the THz yield drops by a factor ≈ 5 due to the lower plasma density.

Figures 12(c)–12(h) illustrate the associated angular THz spectra computed at the distances for which the growth of the THz energy plotted in Fig. 12(b) is maximum. The reference case [Fig. 12(c)] exhibits a conical emission at angles $2.5^\circ < \Theta < 4^\circ$ and extends up to 60 THz. The THz spectrum in the spherical case [Fig. 12(d)] appears to be similar. However, it presents a broadening up to 75 THz, which we attribute to strong nonlinearities associated with the local density peaks observed in Fig. 12(a). Astigmatism [Figs. 12(e) and 12(f)] and coma [Figs. 12(g) and 12(h)] display a reduction of the THz spectral width ($\nu < 45\,\mathrm{THz}$). In the former case, we observe that the radiated wave appears rather axisymmetric despite the asymmetric character of astigmatism. It presents a strong on-axis contribution at low frequencies ($\nu < 20\text{–}25\,\mathrm{THz}$) and a conical emission at $\Theta \approx 4^\circ$ in the upper part of the spectrum ($\nu > 25\,\mathrm{THz}$). In the coma case, the azimuthally varying plasma shape renders the THz spectrum asymmetric with different frequency bandwidths for positive and negative values of Θ. This spectrum comprises on-axis emission for $\nu < 35\text{–}40\,\mathrm{THz}$ and conical emission for $\nu > 40\,\mathrm{THz}$ at angles between 2° and 3° in absolute value.

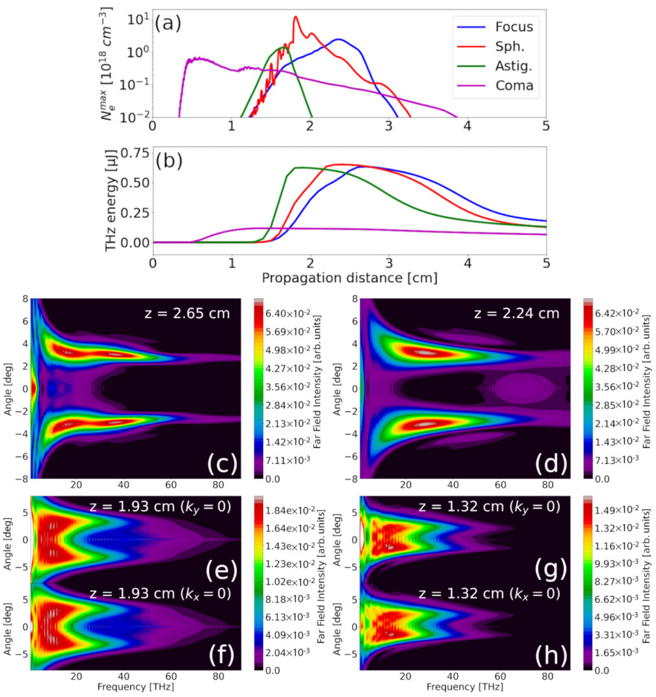

FIG. 12. Top: (a) Maximum electron density and (b) THz energy ($\nu < 90\,\mathrm{THz}$) along z in the reference (focus) case (blue curve), with sphericity (red curve), astigmatism (green curve), and coma aberration (magenta curve). Bottom: Angular THz spectra calculated with the UPPE code (c)–(e) and (g) in the (x, z) plane and (f) and (h) in the (y, z) plane (c) in the focus case at $z = 2.65$ cm, (d) in the sphericity case at $z = 2.24$ cm, (e) and (f) for astigmatism at $z = 1.93$ cm, and (g) and (h) for coma at $z = 1.32$ cm.

For comparison, we integrated our augmented model to reproduce these spectra. The parameters used for its integration are summarized in Table I. We have selected our spectral profiles $A_J(\omega)$ so that they remain close to the transversely integrated UPPE THz spectra [see, e.g., solid blue curve in Fig. 2]. Here, only a plasma driver is accounted for in our test spectral profile. Introducing OA only shortens the bandwidth for asymmetric (e.g., astigmatism) aberrations, as exemplified by Figs. 13(a) and 13(b).

TABLE I. Parameters used to integrate our augmented model for conical emission in the focused regime for LP-P laser pulses with OAs.

	Focus	Sphericity	Astigmatism	Coma
z_p (cm)	2	1.5	1.8	0.8
N_e^{eff} ($10^{18}\,\mathrm{cm}^{-3}$)	0.2	0.4	0.3	0.01
L (mm)	7	5	3	10
l_d (mm)	3.9	2.1	2.8	20

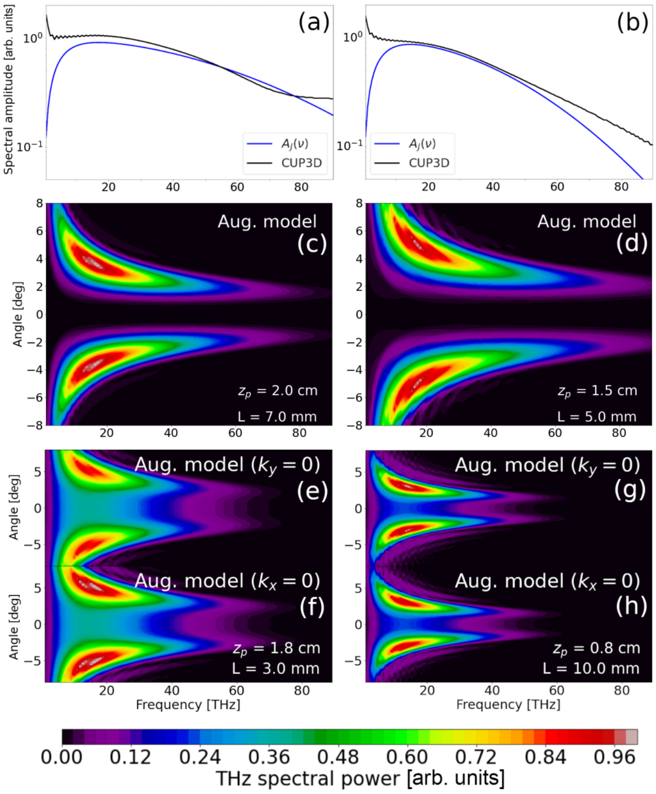

FIG. 13. Transversely integrated THz spectra of Fig. 12 (black curves) and profiles $A_J(\omega)$ (blue curves) chosen to integrate our conical emission model (a) in the sphericity case and (b) the astigmatism case. (c)–(h) Angular THz spectra along (c)–(e) and (g) $k_y = 0$ and (f) and (h) $k_x = 0$ estimated from our augmented conical emission model for a laser propagation affected by (c) no optical aberration (OA), i.e., focus only, (d) sphericity, (e) and (f) astigmatism, and (g) and (h) coma aberration. The parameters used are summarized in Table I.

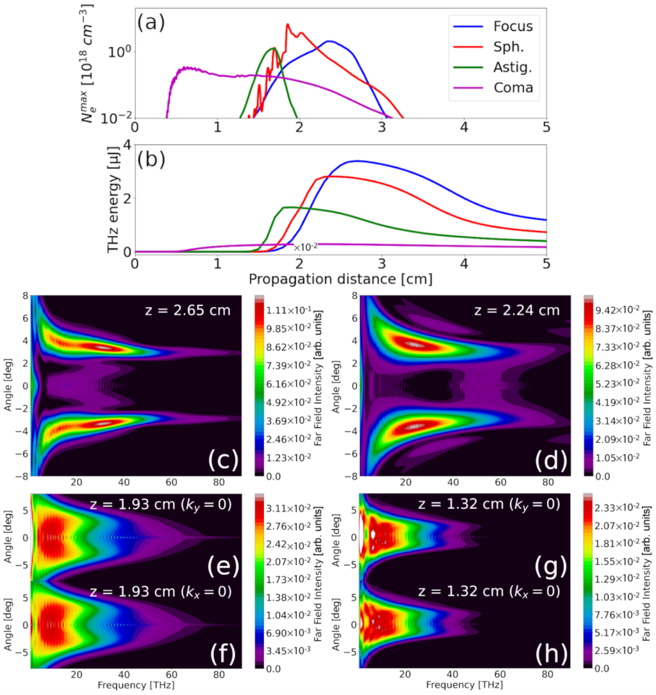

FIG. 14. (a) and (b) Same quantities as in Fig. 12 but for circular polarization–same (CP-S) pulse configuration. (c)–(h) Corresponding angular THz spectra calculated by UPPE (c)–(e) and (g) along $\mathbf{e_x}$ and (f) and (h) along $\mathbf{e_y}$ (c) in the reference case at $z = 2.65$ cm, (d) for sphericity at $z = 2.24$ cm, (e) and (f) for astigmatism at $z = 1.93$ cm, and (g) and (h) for coma at $z = 1.32$ cm.

Figure 13(c) plots the angular THz spectrum estimated by our augmented model for the focus (reference) case. The distance z_p reached by our linear preprocessor is chosen to match beam size and peak intensity similar to those developed by the UPPE runs. The predicted emission angles $\sim$2.5°–3° are in reasonable agreement with those of our UPPE simulations [see Fig. 12(c)]. The sphericity case, shown in Fig. 13(d), describes a conical emission very similar to that of the reference case and predicts angles of $\sim$3°–4°. In agreement with the UPPE calculations, these two figures show that sphericity has little impact on the produced THz spectrum. For astigmatism [Figs. 13(e) and 13(f)], our model reproduces spectral narrowing and relevant on-axis components. However, it slightly overestimates the spectral asymmetries by amplifying more azimuthal variations (up to $\approx 9\%$ in amplitude). These asymmetries are due to the terms $I_S^{\pm}(k_x, k_y)$, which ignore nonlinear propagation effects attached to Kerr self-focusing and plasma defocusing; the latter locally modify the spatiotemporal distributions of the laser pulse and the plasma channel along z.

Nonetheless, the THz emission angles ($\Theta \approx 4°$) are correctly restored. In the case of coma [see Figs. 13(g) and 13(h)], asymmetries emerging in the UPPE spectra are partially reproduced. They are also associated with the asymmetric diffraction caused by the term $J_{\text{tr}}(\mathbf{r}_\perp)$. Discrepancies with the UPPE simulation data can again be attributed to the nonlinear distortion of the plasma channel geometry omitted in our model. The overall spectral dynamics predicted by our model are nevertheless consistent with the UPPE simulation results, namely, a conical emission at angles $\Theta \approx 3°$, with a nonnegligible on-axis contribution as $L \lesssim l_d$.

B. CP-S polarization

We performed a similar study for circularly polarized laser pulses using the same laser-air parameters, except for the pump polarization state. We did not observe major modifications in the nonlinear laser fluency patterns calculated by UPPE for the four configurations of interest. We observed that the geometries of the laser beam and plasma remained similar to Fig. 11, i.e., in the present focused geometry, the laser polarization barely modifies pulse propagation in the presence of OAs.

Figure 14(a) illustrates the axial evolutions of the maximum electron densities reached without OA (focus, blue curve), with sphericity (red curve), astigmatism (green curve), and coma (magenta curve). Again, the peak plasma dynamics are very similar to those observed in the LP-P configuration. Figure 14(b) shows the related THz energy. We retrieve the well-known property following which CP-S laser pulses strongly increase the THz yield compared with their LP-P counterpart [60]. Without OA (blue curve), the THz energy is enhanced by a factor ≈6. This property holds with sphericity

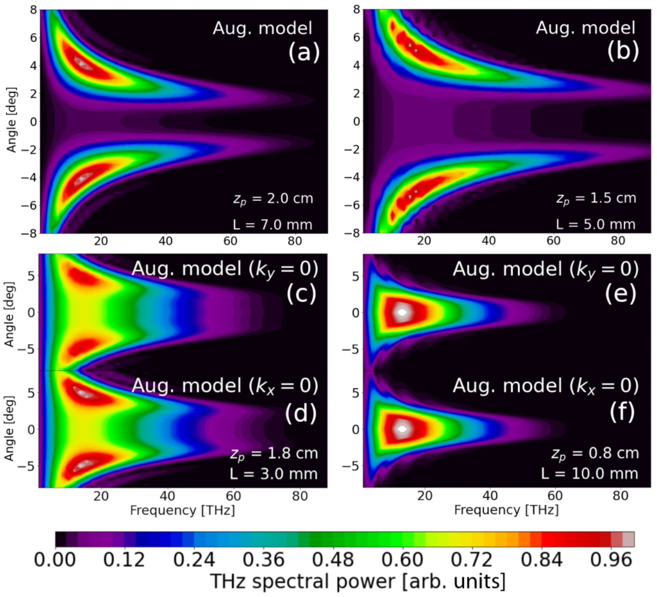

FIG. 15. Same quantities as in Fig. 13(c)–13(h) but for a CP-S laser pulse.

(red curve, ≈ × 4) and astigmatism (green curve, ≈×3), even if these two configurations significantly reduce the laser-to-THz conversion efficiency compared with the reference case. Coma aberration (magenta curve) is again harmful for THz radiation due to its detrimental action on the generated electron density.

Figures 14(c)–14(h) illustrate the associated angular THz spectra. These are close to the LP-P case, although with slightly narrower frequency bandwidth, which we attribute to relatively weaker nonlinearities. The action of astigmatism and coma on the THz distribution [see Figs. 14(e)–14(h)] is close to the LP-P case, although with a less pronounced asymmetry at negative angles in the coma case. Hence, LP-P and CP-S laser beams provide comparable THz emission patterns.

Let us now integrate our conical emission model. We assume that the CP-S polarization state barely modifies the parameters L and $N_e^{\rm eff}$ so that the values presented in Table I can be reused here. The $A_J(\omega)$ factors were checked to remain similar to those used in the LP-P configuration.

Figure 15 plots the results of our model. Angular spectra appear very close to those calculated in the LP-P case, confirming again that laser polarization has a limited impact on conical emission. The overall angular spectra for asymmetric aberrations reasonably agree with their UPPE counterparts in the predicted spectral extent and production of on-axis components. We observe, however, a few discrepancies in the on-axis contributions, which are attributed to a strong dependence of the THz spectrum on the phase $\phi(\mathbf{r}_\perp)$ when $L \approx l_d$. We again emphasize that, because the nonlinear responses of the medium alter the laser pulse during propagation, our model can overestimate some asymmetries in the THz spectra, e.g., for astigmatism [see Figs. 15(c) and 15(d)]. These asymmetries disappear in the coma case [Figs. 15(e) and 15(f)] that amplifies on-axis contribution and agrees better with the UPPE spectra.

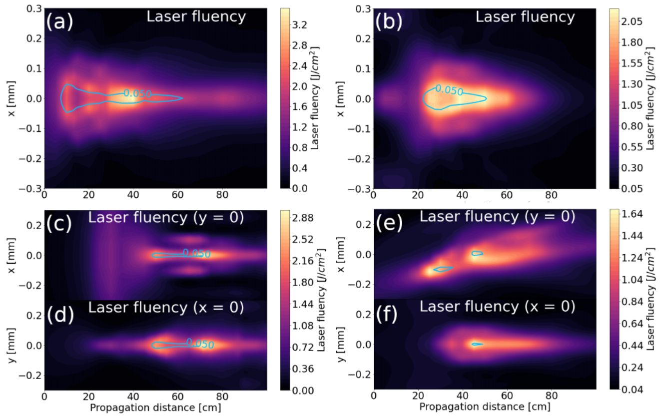

FIG. 16. Laser fluency maps calculated in filamentation regime by the UPPE code (a)–(c) and (e) in the (x, z) plane and (d) and (f) in the (y, z) plane (a) in the reference (focus) case, (b) with sphericity, (c) and (d) astigmatism, and (e) and (f) coma. The blue isocontours represent the isodensities $N_e^{\max} = 5 \times 10^{16}\,{\rm cm}^{-3}$.

C. Influence of optical aberrations in filamentation regime

To explore THz emission in the filamentation regime modified by adaptive optics, we performed UPPE simulations of LP-P laser pulses without OA (focus), with sphericity ($c_4^0 =$ 10 nm), astigmatism ($c_2^2 = 150$ nm), and coma ($c_3^{-1} = 100$ nm). Our 34 fs, two-color laser pulses now have a 2.5 mm initial radius and 1.5 mJ energy, and they are loosely focused with $f = 2.6$ m (equivalent to $c_2^0 = 300$ nm) in air. These simulations required using the linear preprocessor to propagate the laser pulses up to the threshold intensity of the first nonlinearities before using them as input data for the UPPE code. Laser beams without OA and with sphericity, astigmatism, and coma were propagated over 2.3, 1.7, 1.7, and 1.5 m, respectively. The value of the distance z where nonlinear propagation begins was always set to $z = 0$ by convention.

Figure 16 shows the laser fluency calculated with UPPE. The reference case [Fig. 16(a)] displays a plasma zone that extends over several tens of centimeters. Kerr self-focusing–plasma-defocusing cycles induce deviations from the patterns shown in Fig. 11, particularly for pulses affected by asymmetric aberrations. The hollow zones observed in the reference case and with sphericity [Fig. 16(a) and 16(b)] at $z \approx 15$ and 30 cm, respectively, indicate a replenishment dynamics [86]. Unlike the focused regime, despite the presence of astigmatism over a long propagation range, a rather axisymmetric filament develops over the propagation axis. In addition, Figs. 16(e) and 16(f) for coma contain fewer hot spots than the fluency patterns observed in Figs. 11(e) and 11(f). We conclude that, in the filamentation regime, the propagation dynamics is dominated by the nonlinear balance between Kerr self-focusing and plasma defocusing, and linear effects due to OA are less important.

Figure 17(a) describes the longitudinal evolutions of $N_e^{\max}$ in the reference case (blue curve), with sphericity (red curve), astigmatism (green curve), and coma (magenta curve). The differences in the plasma onset distances are mainly due to the selected final distances of the preprocessed linear propagation runs, which vary from one case to another. Focus and spheric-

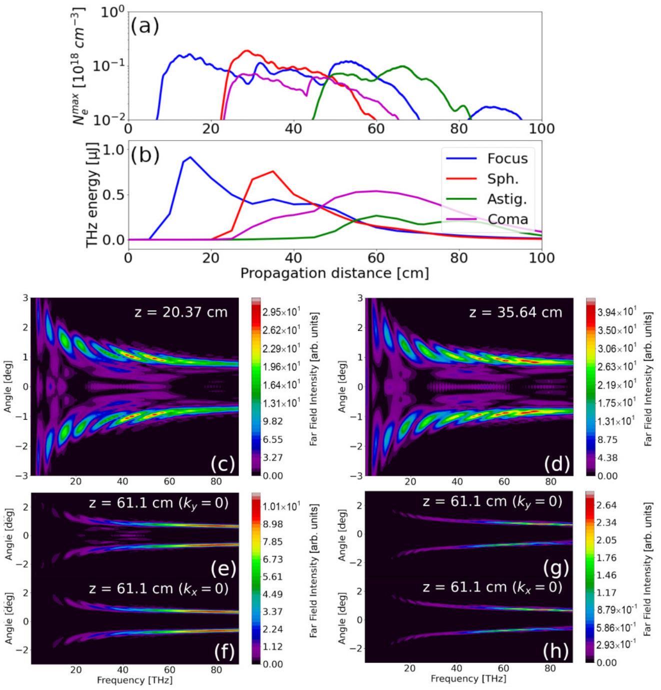

FIG. 17. Top: (a) Maximum electron density and (b) THz energy ($\nu < 90$ THz) along z in the reference case (focus, blue curve), with sphericity (red curve), astigmatism (green curve), and coma (magenta curve). Bottom: Angular THz spectra calculated with UPPE (c)–(e) and (g) along $\mathbf{e_x}$ and (f) and (h) along $\mathbf{e_y}$ (c) in the reference case at $z = 20.4$ cm, (d) with sphericity at $z = 35.6$ cm, (e) and (f) astigmatism at $z = 61.1$ cm, and (g) and (h) coma at $z = 61.1$ cm.

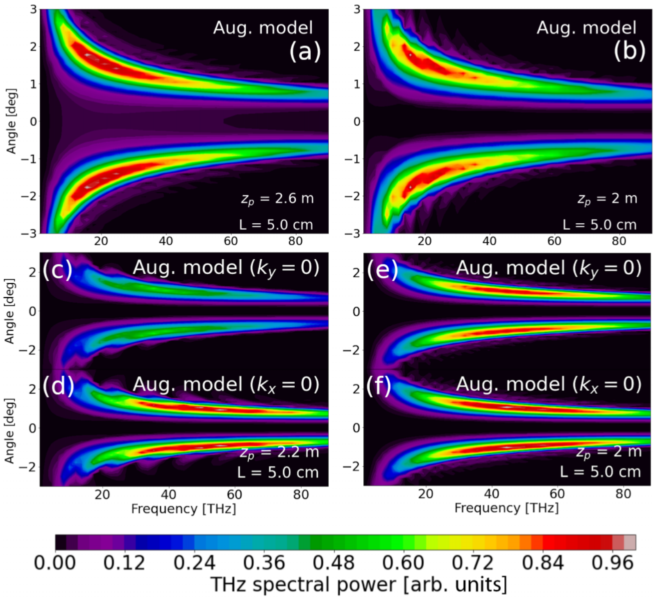

FIG. 18. Angular THz spectra (a)–(c) and (e) along $\mathbf{e_x}$ and (d) and (f) along $\mathbf{e_y}$ estimated using our augmented conical emission model for a laser propagation affected by (a) no OA (lens of 2.6 m focal length), (b) sphericity, (c) and (d) astigmatism, and (e) and (f) coma. Key parameters used for integration are detailed in Table II.

ity induce comparable maximum densities, although the latter reduces the plasma length. On the other hand, asymmetric aberrations reduce plasma density levels by a factor of ≈ 2 and decrease the length of the plasma zone. Figure 17(b) plots the produced THz energy ($\nu < 90$ THz). We observe that all aberrations reduce the production of THz yield. OAs are thus generally harmful for THz generation in the filamentation regime, like their impact in the focused regime.

UPPE angular THz spectra are presented in Figs. 17(c)–17(h). In both the reference case [Fig. 17(c)] and with sphericity [Fig. 17(d)], the THz radiation exhibits a relatively flat spectrum up to 90 THz, which is typical of the filamentation regime. Additionally, the emission angle remains nearly constant over a wide frequency bandwidth. Astigmatism and coma illustrated by Figs. 17(e), 17(f) and 17(g), 17(h) modify the spectrum with an almost zero contribution at low frequencies ($\nu < 15$–20 THz). Like in the focused regime, astigmatism does not induce any asymmetry in the THz intensity radiated in the filamentation regime. Coma tends to slightly unbalance THz emission between positive and negative Θ because of the misalignment of the plasma channel with respect to the optical axis. The observed THz emission angles remain analogous to those of the reference case in the filamentation regime; although affected by OA, the effective plasma density is weaker. Moreover, the plasma length in this regime always satisfies the condition $L \gg l_d$, ensuring perfectly conical emission in the far field. The oblique lobes, particularly visible at low frequencies in the spectra of Figs. 17(c) and 17(d), are a numerical artifact due to a coarser resolution in Θ at low frequency ν.

To end with, we integrated our conical emission model using the parameters summarized in Table II. The spectral distribution $A_J(\omega)$ (dashed blue curve in Fig. 2) was chosen in each case to approach the broadband UPPE spectral profiles, which did not change significantly by adding OA. These include 32% of Kerr contribution in amplitude (10% in energy ratio) extending till ~70 THz. The results provided by our model are illustrated in Fig. 18. As in the UPPE simulations, OAs have no significant impact on the THz emission angles ($\Theta = 1^\circ$–2°), which are correctly restored here. Despite the overestimated asymmetries in Figs. 18(c) and 18(d), our augmented model restores the vanishing of the low-frequency region for astigmatism and coma, together with the main trends of the UPPE spectrum.

TABLE II. Parameters used to integrate our augmented conical emission model in filamentation regime with OAs.

	Focus	Sphericity	Astigmatism	Coma
z_p (m)	2.6	2	2.2	2
N_e^{eff} (10^{18} cm^{-3})	0.01	0.01	0.01	0.01
L (cm)	5	5	5	5
l_d (cm)	2	2	2	2

V. CONCLUSIONS

In this paper, we have revisited the problem of far-field conical THz emission produced by two-color-driven air plasmas in the two main configurations of interest met in current experiments, namely, the focused and filamentation propagation regimes. The numerical patterns computed from a 3D UPPE solver were systematically compared with the results of simpler descriptions, inspired by the pioneering model of You *et al.* [48]. To account for transverse laser variations that can potentially alter the spatial geometry of the emitting source (plasma or Kerr response), we derived a so-called *augmented* conical emission model able to satisfactorily reproduce angular THz spectra provided by UPPE simulations. This model is called *augmented* because it still relies on the key parameters found by You *et al.* [48]. Yet, it takes into account three other crucial quantities, namely, (i) the spectral distribution of the THz source in the nonlinear propagation regime of interest, (ii) the transverse profile and phase of the beam when it undergoes lensing effect or more complex phase distortions such as, e.g., those induced by deformable mirrors, and (iii) Kerr contribution to the overall THz radiation when self-focusing may become relevant, e.g., in the long-range filamentation regime. Our augmented model also addressed the role of pulse temporal envelopes, which has been shown to be relatively limited, and it could be generalized to circularly polarized two-color pulses.

By carefully comparing the results obtained from our augmented model with comprehensive UPPE simulation data, we find an alternative to running heavy computations evaluating angular THz spectra to interpret current experiments. Indeed, it appears sufficient to model a class of spectral profiles appropriately with respect to the targeted nonlinear propagation regime (tightly or loosely focused geometry) and appreciate the weight of the Kerr contribution to get reliable angular radiation patterns. Alternatively, LC-computed spectra could have been used, or if available, 3D UPPE spectral profiles could directly be implemented in the spectral amplitude $A(\omega)$. However, we have shown that simple test functions for the spectral distributions allow one to obtain valuable radiated intensities.

Importantly, instead of selecting a single radiated spectrum at a given propagation distance, we probed the whole spectral dynamics by examining changes in the radiated patterns for various plasma lengths around the dephasing length l_d. It appears that a good knowledge of the spectral dynamics along the propagation range covering the THz emitting zone is much more instructive than only analyzing the spectrum at the end of the plasma channel.

In connection with this property, our 3D UPPE simulations display evidence that the choice of the actual plasma length L must be given by the length over which THz field emission takes place. This length is generally much shorter than the overall plasma extent along the optical axis. By computing the evolution of the relative phase between the two laser harmonics numerically along this effective plasma length (Fig. 3), we have proven that, in focused propagation, L remains close to l_d, which justifies why most of the radiated spectra measured in such emission regimes [47,53,55,87] contain both on-axis emissions at small THz frequencies and net conical emission at higher frequencies. In contrast, a collimated or loosely focused propagation promotes plasma lengths $L \gg l_d$ and leads to conical emission in the entire THz frequency range. For the baseline laser-air parameters used in this paper, THz emission angles at frequencies $\nu > 10$ THz were found to be limited to 4°–5° in the focused regime and to barely exceed 2° in the filamentation regime.

Finally, we performed exhaustive UPPE simulations of laser pulses distorted by optical aberrations, the results of which are in reasonable agreement with our augmented model. We found that, although transverse phase distortions foster a decrease in the THz energy yield and bandwidth, the maximum emission angles remain comparable with those promoted by aberrationless laser beams. These results thus indicate that OAs should be avoided to optimize THz generation. OAs were found to have a similar impact on the THz waveshapes for circularly and linearly polarized pump pulses.

In conclusion, we believe that we have provided the terahertz community with a deeper understanding of the THz spectral dynamics and additional tools to predict angular THz radiation patterns delivered by two-color air plasmas in future experiments.

The data supporting our findings are available within this paper. Complementary data can be made available from the corresponding authors upon reasonable request.

ACKNOWLEDGMENTS

We acknowledge support from the Agence Nationale de la Recherche and Agence Innovation Défense (AID/ANR - 19 - ASMA - 007) and the Grand Equipement National de Calcul Intensif (GENCI project A0120507594).

APPENDIX A: THz EMISSION MODEL

Here, we establish a general conical emission model that includes laser envelope profiles in time and in the transverse plane. Let t be the time variable and $\mathbf{r}$ be the position of the THz wave detector. The origin of the frame is located at the center of the plasma with length L assumed to be finite. In what follows, Θ corresponds to the polar angle at which the radiation is emitted with respect to the optical axis; Φ is the azimuthal angle.

Helmholtz's theorem gives the vector potential $\mathbf{A}(\mathbf{r}, t)$ emitted by a plasma source of volume V with current density $\mathbf{J}(\mathbf{r}, t)$ as

$$\mathbf{A}(\mathbf{r}, t) = \frac{\mu_0}{4\pi} \int_V d^3\mathbf{r}' \frac{\mathbf{J}(\mathbf{r}', t')}{|\mathbf{r} - \mathbf{r}'|}, \tag{A1}$$

where $t' = t - |\mathbf{r} - \mathbf{r}'|/c$ corresponds to the retarded time at which the signal received at time t was produced. The associated electric field $\mathbf{E}(\mathbf{r}, t)$, in the absence of a scalar potential, follows from

$$\mathbf{E}(\mathbf{r}, t) = -\frac{\mu_0}{4\pi} \int_V d^3\mathbf{r}' \frac{\partial_t \mathbf{J}(\mathbf{r}', t')}{|\mathbf{r} - \mathbf{r}'|}, \tag{A2}$$

and the magnetic field from

$$\mathbf{B}(\mathbf{r}, t) = \frac{\mu_0}{4\pi} \int_V d^3\mathbf{r}' \frac{\nabla \times \mathbf{J}(\mathbf{r}', t')}{|\mathbf{r} - \mathbf{r}'|}. \tag{A3}$$

For the photocurrent mechanism considered here, it is safe to assume that the relevant current density is transverse and that no charge separation occurs ($\nabla \cdot \mathbf{J} = 0$), which justifies the use of Eq. (A2) to compute the radiated far-field power. We note that, for the transition Cherenkov mechanism [51,88–92], where the relevant current density is longitudinal and $\nabla \cdot \mathbf{J} \neq 0$ produces a charge density, one would need to account for a scalar potential in Eq. (A2) or resort to Eq. (A3).

The temporal Fourier transform of Eq. (A2) leads to

$$\widehat{\mathbf{E}}(\mathbf{r}, \omega) = \frac{i\omega\mu_0}{4\pi} \int_V d^3\mathbf{r}' \frac{\exp(i|\mathbf{r} - \mathbf{r}'|\omega/c)}{|\mathbf{r} - \mathbf{r}'|} \widehat{\mathbf{J}}(\mathbf{r}', \omega). \tag{A4}$$

We assume that the distance between the plasma and the detector is large compared with the filament dimensions, that is, $|\mathbf{r}| \gg |\mathbf{r}'|$. Cartesian, cylindrical, and spherical coordinates are written (x, y, z), (r, φ, z), and (r, Θ, Φ). The notation $'$ applies to the local coordinates in the plasma. The far-field assumption leads to the simplification:

$$|\mathbf{r} - \mathbf{r}'| \simeq r - \frac{\mathbf{r}' \cdot \mathbf{r}}{r} = r - \frac{c}{\omega}\mathbf{k}_\perp \cdot \mathbf{r}'_\perp - z' \cos\Theta, \tag{A5}$$

with $\mathbf{k}_\perp = (\omega/c)(\sin\Theta\cos\Phi, \sin\Theta\sin\Phi)$, providing Eq. (24).

To evaluate the source terms $\mathbf{J}_e(\mathbf{r}, t)$ and $\mathbf{P}_K(\mathbf{r}, t)$ in Eq. (25) for a two-color laser pulse, we employ the general expression of the LP-P two-color laser field [Eq. (26)] and apply the assumptions discussed in the main text. The free-electron contribution $\mathbf{J}_e(\mathbf{r}, t)$ is calculated using the toy ionization rate and assuming a small ionization yield:

$$W(E) = CE^2(t), \quad N_e(t) = CN_a \int_{-\infty}^{t} E^2(t')dt'. \tag{A6}$$

The square of the LP-P two-color laser field Eq. (26) with the assumptions discussed in the main text reads

$$\begin{aligned} E_L^2(\mathbf{r}, t) = {} & \mathcal{E}_1^2 \cos^2[\omega_0 t_1' + \phi_1] + \mathcal{E}_2^2 \cos^2[2\omega_0 t_2' + \phi_2] \\ & + 2\mathcal{E}_1\mathcal{E}_2 \cos[2\omega_0 t_2' + \phi_2] \cos[\omega_0 t_1' + \phi_1], \end{aligned} \tag{A7}$$

where we omitted the arguments of $\mathcal{E}_1(\mathbf{r}_\perp, t_1')$, $\mathcal{E}_2(\mathbf{r}_\perp, t_2')$, $\phi_1(\mathbf{r}_\perp)$, and $\phi_2(\mathbf{r}_\perp)$ for conciseness. For the plasma term, straightforward integration of Eq. (A6) leads to linear and sine temporal dependencies in time when slowly varying envelopes are assumed. The product $N_e(t)\mathbf{E}_L(t)$ thus contains quasistationary contributions in the terms:

$$\frac{CN_a}{4\omega_0}\mathcal{E}_1^2 \sin[2\omega_0 t_1' + 2\phi_1]\mathcal{E}_2 \cos[2\omega_0 t_2' + \phi_2]\mathbf{e}_\mathbf{x},$$

and

$$\frac{CN_a}{\omega_0}\mathcal{E}_1\mathcal{E}_2 \sin[\omega_0(2t_2' - t_1') + \phi_2 - \phi_1]\mathcal{E}_1 \cos[\omega_0 t_1' + \phi_1]\mathbf{e}_\mathbf{x}.$$

The treatment of the Kerr term proceeds similarly from Eq. (7) without integration in time and, therefore, only contains cosine contributions. After retaining only the quasistationary terms, the two potential THz sources can then be expressed as

$$\begin{aligned} (\partial_t + \nu_c)\mathbf{J}_{e,\mathrm{THz}}(\mathbf{r}, t) = {} & J_{e,0}\, \mathcal{E}_1^2(\mathbf{r}_\perp, t_1')\mathcal{E}_2(\mathbf{r}_\perp, t_2') \\ & \times \sin[\Delta k z + \phi(\mathbf{r}_\perp)]\mathbf{e}_\mathbf{x} \end{aligned} \tag{A8}$$

using $J_{e,0} = 3CN_a e^2/(8m_e\omega_0)$, and

$$\mathbf{P}_{K,\mathrm{THz}}(\mathbf{r}, t) = P_{K,0}\, \mathcal{E}_1^2(\mathbf{r}_\perp, t_1')\mathcal{E}_2(\mathbf{r}_\perp, t_2') \cos[\Delta k z + \phi(\mathbf{r}_\perp)]\mathbf{e}_\mathbf{x}, \tag{A9}$$

with $P_{K,0} = 3\varepsilon_0\chi^{(3)}/4$, $\Delta k = \pi/l_d$, and l_d denoting the dephasing length given in Eq. (16). With the assumption of separable laser envelopes in space and time [Eq. (27)], we can simplify the relations in Eqs. (A8) and (A9), and the unified source term $\widehat{\mathbf{J}}(\mathbf{r}, \omega)$, cf. Eq. (25), reads

$$\widehat{\mathbf{J}}(\mathbf{r}, \omega) = \widehat{\mathbf{J}}_0(\mathbf{r}, \omega)J_{\mathrm{tr}}(\mathbf{r}_\perp)\mathcal{F}_t\big[\mathcal{E}_{ax,1}^2(t_1')\mathcal{E}_{ax,2}(t_2')\big](\omega), \tag{A10}$$

where $J_{\mathrm{tr}}(\mathbf{r}_\perp) = \mathcal{E}_{\mathrm{tr},1}^2(\mathbf{r}_\perp)\mathcal{E}_{\mathrm{tr},2}(\mathbf{r}_\perp)$ [see Eq. (37)], and

$$\begin{aligned} \widehat{\mathbf{J}}_0(\mathbf{r}_\perp, z, \omega) = {} & \frac{J_{e,0}}{\nu_c - i\omega} \sin[\Delta k z + \phi(\mathbf{r}_\perp)]\mathbf{e}_\mathbf{x} \\ & - i\omega P_{K,0} \cos[\Delta k z + \phi(\mathbf{r}_\perp)]\mathbf{e}_\mathbf{x}. \end{aligned} \tag{A11}$$

Here, $\mathcal{F}_t$ refers to Fourier transform in time, and using $t'_{j=\{1,2\}} = t - zn(j\omega_0)/c$, we can rewrite

$$\begin{aligned} \mathcal{F}_t[\mathcal{E}_{ax,1}^2(t_1')\mathcal{E}_{ax,2}(t_2')](\omega) &= \int \mathcal{E}_{ax,1}^2(t_1')\mathcal{E}_{ax,2}(t_2') \exp(i\omega t)dt \\ &= \exp[ikn(\omega_0)z] \int \mathcal{E}_{ax,1}^2(t_1') \\ &\quad \times \mathcal{E}_{ax,2}(t_1' - \gamma) \exp(i\omega t_1')dt_1', \end{aligned}$$

with $k = \omega/c$ being the THz wave number in vacuum and $\gamma = \pi z/(2\omega_0 l_d)$. For not too short pulses and plasma lengths of at most a few l_d, we can neglect γ and therefore the z-dependency of the integral. Thus, we have established that

$$\mathcal{F}_t\big[\mathcal{E}_{ax,1}^2(t_1')\mathcal{E}_{ax,2}(t_2')\big](\omega) \approx \exp[ikn(\omega_0)z]C_{\mathrm{env}}(\omega), \tag{A12}$$

with

$$C_{\mathrm{env}}(\omega) = \int \mathcal{E}_{ax,1}^2(t_1')\mathcal{E}_{ax,2}(t_1') \exp(i\omega t_1')dt_1'. \tag{A13}$$

While this expression is valid for arbitrary (slowly varying) pulse envelopes, it is instructive to inspect it for Gaussian envelopes:

$$\mathcal{E}_{ax,j}(t) \propto \exp\left[-\frac{\left(t - t_c^j\right)^2}{t_j^2}\right], \tag{A14}$$

with t_j being the duration of the jth color envelope and t_c^j its temporal offset. After straightforward computations, we obtain a Gaussian power spectrum:

$$\begin{aligned} C_{\mathrm{env}}(\omega) \propto {} & \frac{t_1 t_2\sqrt{\pi}}{t_{\mathrm{eq}}} \exp\left(-\frac{2\Delta t^2}{t_{\mathrm{eq}}^2}\right) \exp\left[i\omega\left(t_c^1 - \Delta t\frac{t_1^2}{t_{\mathrm{eq}}^2}\right)\right] \\ & \times \exp\left(-\frac{t_1^2 t_2^2}{4t_{\mathrm{eq}}^2}\omega^2\right), \end{aligned} \tag{A15}$$

where $t_{\mathrm{eq}} = \sqrt{2t_2^2 + t_1^2}$, and $\Delta t = t_c^1 - t_c^2$ is the temporal separation of the two envelopes. Most notably, the amplitude strongly decreases with increasing Δt^2. Interestingly, deviations from the above slowly varying assumptions and $\omega \ll \omega_0$ would produce additional contributions of orders $\Delta t L/(\omega_0 t_{\mathrm{eq}}^2 l_d)$ and $\omega\lambda_{\mathrm{THz}}/(\omega_0 l_d)$, respectively, in the argument of the sinc function of Eq. (19). Deviations from the above requirement $\omega\gamma \ll 1$ would introduce a z-dependent correction $\exp(-i\gamma\omega t_1^2/t_{\mathrm{eq}}^2)$ into C_{env}. For a 0.8 μm fundamental pulse, this contribution remains small for THz frequencies < 60 THz (120 THz) if $L \leqslant 4\, l_d$ (respectively, $L \leqslant 2\, l_d$).

The source term $\widehat{\mathbf{J}}(\mathbf{r}, \omega)$ hence reads

$$\widehat{\mathbf{J}}(\mathbf{r}, \omega) \approx \widehat{\mathbf{J}}_0(\mathbf{r}, \omega) J_{\mathrm{tr}}(\mathbf{r}_\perp) \exp[ikzn(\omega_0)] C_{\mathrm{env}}(\omega). \tag{A16}$$

By injecting Eq. (A16) into Eq. (24), the radiated electric field takes the form:

$$\widehat{\mathbf{E}}(r, \Theta, \Phi, \omega) = \frac{\mu_0}{4\pi r} \exp(ikr) \sum_{j=J,K} C_j(\Theta, \Phi, \omega), \tag{A17}$$

where

$$C_{J,K}(\Theta, \Phi, \omega) = A_{J,K}(\omega) \mathbf{I}_{J,K}(\Theta, \Phi, \omega). \tag{A18}$$

Here, $A_{J,K}(\omega)$ are the THz spectral profiles associated with the photocurrents and Kerr response:

$$A_J(\omega) = i\omega C_{\mathrm{env}}(\omega) \frac{J_{e,0}}{\nu_c - i\omega}, \tag{A19}$$

$$A_K(\omega) = \omega^2 C_{\mathrm{env}}(\omega) P_{K,0}, \tag{A20}$$

while $\mathbf{I}_{J,K}(\Theta, \Phi, \omega)$ describes the interferences between the THz waves generated along the plasma channel:

$$\mathbf{I}_J(\Theta, \Phi, \omega) = \int_{-L/2}^{L/2} dz' \exp\{ikz'[n(\omega_0) - \cos\Theta]\} \frac{\exp(i\Delta kz') I_S^+(\Theta, \Phi, \omega) - \exp(-i\Delta kz') I_S^-(\Theta, \Phi, \omega)}{2i} \mathbf{e}_\mathbf{x},$$

$$\mathbf{I}_K(\Theta, \Phi, \omega) = \int_{-L/2}^{L/2} dz' \exp\{ikz'[n(\omega_0) - \cos\Theta]\} \frac{\exp(i\Delta kz') I_S^+(\Theta, \Phi, \omega) + \exp(-i\Delta kz') I_S^-(\Theta, \Phi, \omega)}{2} \mathbf{e}_\mathbf{x}.$$

The quantities $I_S^\pm(\Theta, \Phi, \omega)$ refer to the transverse integral contributions to the THz spectrum:

$$I_S^\pm(\Theta, \Phi, \omega) = \iint d^2\mathbf{r}'_\perp J_{\mathrm{tr}}(\mathbf{r}'_\perp) \exp[\pm i\phi(\mathbf{r}'_\perp)] \times \exp(-i\mathbf{k}_\perp \cdot \mathbf{r}'_\perp). \tag{A21}$$

The functions $I_S^\pm(\Theta, \Phi, \omega)$ can be rewritten as

$$I_S^\pm(\Theta, \Phi, \omega) = \mathcal{F}_\perp\{J_{\mathrm{tr}}(\mathbf{r}_\perp) \exp[\pm i\phi(\mathbf{r}_\perp)]\}(\Theta, \Phi, \omega), \tag{A22}$$

where $\mathcal{F}_\perp$ represents the transverse Fourier transform.

It can be checked that the elementary transformations:

$$\sin[\Delta kz + \phi(\mathbf{r}_\perp)]\mathbf{e}_\mathbf{x} \to \left\{\begin{matrix} \sin[\Delta kz + \phi(\mathbf{r}_\perp)] \\ \cos[\Delta kz + \phi(\mathbf{r}_\perp)] \end{matrix}\right\}, \tag{A23}$$

$$\cos[\Delta kz + \phi(\mathbf{r}_\perp)]\mathbf{e}_\mathbf{x} \to \left\{\begin{matrix} \cos[\Delta kz + \phi(\mathbf{r}_\perp)] \\ -\sin[\Delta kz + \phi(\mathbf{r}_\perp)] \end{matrix}\right\}, \tag{A24}$$

allow one to treat CP-S laser pulses similarly, cf. Eq. (2).

Straightforward calculation of the integrals $\mathbf{I}_{J,K}(\Theta, \Phi, \omega)$ gives, for a LP-P laser pulse,

$$\mathbf{I}_J^{\text{LP-P}}(\Theta, \Phi, \omega) = \frac{L}{2}[I_S^+\kappa_+ - I_S^-\kappa_-]\mathbf{e}_\mathbf{x}, \tag{A25}$$

$$\mathbf{I}_K^{\text{LP-P}}(\Theta, \Phi, \omega) = i\frac{L}{2}[I_S^+\kappa_+ + I_S^-\kappa_-]\mathbf{e}_\mathbf{x}, \tag{A26}$$

and for a CP-S pulse,

$$\mathbf{I}_J^{\text{CP-S}}(\Theta, \Phi, \omega) = \frac{L}{2}\begin{pmatrix} I_S^+\kappa_+ - I_S^-\kappa_- \\ I_S^+\kappa_+ + I_S^-\kappa_- \end{pmatrix}, \tag{A27}$$

$$\mathbf{I}_K^{\text{CP-S}}(\Theta, \Phi, \omega) = i\frac{L}{2}\begin{pmatrix} I_S^+\kappa_+ + I_S^-\kappa_- \\ -I_S^+\kappa_+ + I_S^-\kappa_- \end{pmatrix}. \tag{A28}$$

The quantities $\kappa_\pm$ are defined by

$$\kappa_\pm = \mathrm{sinc}(\alpha_\pm), \tag{A29}$$

$$\alpha_\pm = \frac{1}{2}kL\left(n_0 - \cos\Theta \pm \frac{\lambda_{\mathrm{THz}}}{2l_d}\right), \tag{A30}$$

with $\mathrm{sinc}(x) = \sin x/x$, and $k = \omega/c = 2\pi/\lambda_{\mathrm{THz}}$.

Equations (A13), (A25), and (A26) [alternatively, Eqs. (A27) and (A28)] can finally be inserted into Eq. (A17) to obtain the far-field spectral intensity:

$$|\widehat{\mathbf{E}}(r, \Theta, \Phi, \omega)|^2 = \frac{\mu_0^2}{16\pi^2 r^2}\left|\sum_{j=J,K} C_j(\Theta, \Phi, \omega)\right|^2. \tag{A31}$$

We have implicitly assumed that the dephasing length l_d is constant in space, although the source terms of THz radiation include radial variations. This means that like for the model of You *et al.* [48], we need to select an effective electron density level N_e^{eff} to estimate l_d and thus evaluate our model.

Note that, like in Ref. [48], we ignore plasma absorption and opacity in the THz frequency range. These assumptions can be justified as follows. By neglecting the Kerr contribution and focusing on plasma dispersion, Eq. (17) reads

$$\begin{aligned} n^2(\omega) &= n_{\mathrm{opt}}^2(\omega) - \frac{\omega_p^2}{\omega^2(1 + i\nu_c/\omega)} \\ &= n_{\mathrm{opt}}^2(\omega) - \frac{\omega_p^2}{\omega^2 + \nu_c^2} + i\frac{\nu_c}{\omega}\frac{\omega_p^2}{\omega^2 + \nu_c^2}. \end{aligned} \tag{A32}$$

The real and imaginary parts of the medium index are given by

$$\mathrm{Re}[n(\omega)] = \left\{\frac{|n^2(\omega)| + \mathrm{Re}[n^2(\omega)]}{2}\right\}^{1/2}, \tag{A33}$$

$$\Im[n(\omega)] = \left\{\frac{|n^2(\omega)| - \mathrm{Re}[n^2(\omega)]}{2}\right\}^{1/2}. \tag{A34}$$

For $\mathrm{Re}[n^2(\omega)] > 0$, attenuation of THz waves through $\Im[n(\omega)]$ is due to plasma absorption ($\nu_c \approx 3\,\mathrm{THz}$), which recovers the approximation of Kim *et al.* [50] $\Im[n(\omega)] \approx \nu_c\omega_p^2/[2\omega(\omega^2 + \nu_c^2)]$ in the limits $\nu_c/\omega \ll 1$, $n_{\mathrm{opt}}^2(\omega) \approx 1$. At density levels $N_e \lesssim 10^{17}\,\mathrm{cm}^{-3}$, the absorption length $L_a = c/\{\omega\Im[n(\omega)]\}$ is of the order of $\sim 100\,\mu\mathrm{m}$ at $\omega = 2\pi\nu_c$. As typical filaments have a radius of $a \approx 20\,\mu\mathrm{m}$ and THz radiation is emitted at angles $\Theta \approx 5^\circ$, the propagation distance of those waves to exit the plasma is $\approx 200\,\mu\mathrm{m} \sim L_a$, meaning that plasma absorption should already have a limited effect on the emitted THz field. At higher frequencies, L_a quickly increases (∼500 μm at 5 THz), and absorption becomes negligible.

In the lower region of the THz spectrum, $\mathrm{Re}[n^2(\omega)] = n_{\mathrm{opt}}^2(\omega) - \omega_p^2/(\omega^2 + \nu_c^2)$ may become negative. Then the attenuation of the THz waves through $\Im[n(\omega)]$ is due to the plasma opacity. However, this effect barely impacts the forward emitted spectrum, as the THz field is emitted at the front of the plasma, i.e., before the plasma builds up [93,94], so that the local electron density N_e and thus ω_p take smaller values.

Finally, we also discarded plasma resonances due to the radial inhomogeneity of the plasma profile [95,96]. Such resonances indeed manifest for rather high charge densities and when charge separation effects become relevant, which departs from our context. For Gaussian-like smooth density profiles, they are moreover expected to modify the THz spectrum with small amplitude contributions at about half the electron plasma frequency, e.g., < 2 THz for typical electron densities of $N_e = 10^{17}\,\mathrm{cm}^{-3}$, which corresponds to the lowest accessible frequency regions of our numerically computed broadband spectra exceeding 50 THz. We note that such resonant features become important when microplasmas with strong plasma gradients are considered [51,97].

APPENDIX B: DERIVATION OF THE MODEL OF YOU *ET AL.* [48]

The model of You *et al.* [48] and Oh *et al.* [49] [Eq. (18)] can be easily derived from our augmented emission model. Let us assume a homogeneous cylindrical plasma of length L and radius a. Thus, the source term J_{tr} contained in $I_S^{\pm}(\Theta, \Phi, \omega)$ is constant on the disk $\mathcal{D}$ of radius $r_\perp < a$ and zero outside. Moreover, we introduce ϕ_0 as the constant value taken by the phase $\phi(\mathbf{r}_\perp)$. Hence, we can write

$$\begin{aligned} I_S^{\pm} &= \exp(\pm i\phi_0) \iint_{\mathcal{D}} d^2\mathbf{r}'_\perp \exp(-i\mathbf{k}_\perp \cdot \mathbf{r}'_\perp) \\ &= \exp(\pm i\phi_0) \int_0^a dr'_\perp r'_\perp \int_0^{2\pi} d\varphi' \exp(-ik_\perp r'_\perp \cos\varphi') \\ &= 2\pi \exp(\pm i\phi_0) \int_0^a dr'_\perp r'_\perp J_0(k_\perp r'_\perp), \end{aligned}$$

with $J_0(x)$ being the Bessel function of the first kind and rank 0. The simplifications continue by using the identity $\int dx x J_0(x) = x J_1(x)$ [98], where $J_1(x)$ describes the Bessel function of the first kind and rank 1:

$$I_S^{\pm}(\Theta, \omega) = 2\pi \exp(\pm i\phi_0) a^2 \frac{J_1(\beta)}{\beta}, \tag{B1}$$

where we used $k_\perp = k \sin\Theta$ and $\beta = ak \sin\Theta$.

If we now neglect the contribution of the Kerr response to the THz radiation [$A_K(\omega) = 0$], assume that the laser pulse is linearly polarized (LP-P), and $n_{\mathrm{opt}}(\omega_0) = 1$, we can evaluate Eq. (A31) as

$$\begin{aligned} |\widehat{E}(r, \Theta, \omega)|^2 = \frac{\mu_0^2}{16 r^2} a^4 L^2 |A_J(\omega)|^2 \left[\frac{J_1(\beta)}{\beta}\right]^2 \\ \times |\exp(i\phi_0)\kappa_+ - \exp(-i\phi_0)\kappa_-|^2, \end{aligned}$$

where the term depending on $\alpha_\pm$ develops as

$$|\exp(i\phi_0)\kappa_+ - \exp(-i\phi_0)\kappa_-|^2 = \kappa_+^2 + \kappa_-^2 - 2\kappa_+\kappa_- \cos(2\phi_0). \tag{B2}$$

The far-field THz intensity radiated by the plasma thus restores Eq. (18) of You *et al.* [48], where $A(\omega) \equiv A_J(\omega)$.

[1] M. Tonouchi, Cutting-edge terahertz technology, Nat. Photonics **1**, 97 (2007).

[2] N. C. Currie, F. J. Demma, D. D. Ferris Jr., R. W. McMillan, M. C. Wicks, and K. Zyga, Imaging sensor fusion for concealed weapon detection, Invest. Image Process. **2942**, 71 (1997).

[3] J. F. Federici, THz imaging and sensing for security applications—Explosives, weapons and drugs, Semicond. Sci. Technol. **20**, S266 (2005).

[4] B. E. Cole, R. M. Woodward, D. A. Crowley, V. P. Wallace, D. D. Arnone, and M. Pepper, Terahertz imaging and spectroscopy of human skin in vivo, in *Proceedings of the SPIE 4276, Commercial and Biomedical Applications of Ultrashort Pulse Lasers, San Jose, CA, United States* (SPIE, 2001).

[5] R. M. Woodward, V. P. Wallace, D. D. Arnone, E. H. Linfield, and M. Pepper, Terahertz pulsed imaging of skin cancer in the time and frequency domain, J. Biol. Phys. **29**, 257 (2003).

[6] E. Pickwell, B. E. Cole, A. J. Fitzgerald, M. Pepper, and V. P. Wallace, *In vivo* study of human skin using pulsed terahertz radiation, Phys. Med. Biol. **49**, 1595 (2004).

[7] K. Fukunaga, Y. Ogawa, S. Hayashi, and I. Hosako, Terahertz spectroscopy for art conservation, IEICE Electron. Express **4**, 258 (2007).

[8] T. Yasui, T. Tasuda, K. Sawanaka, and T. Araki, Terahertz paintmeter for noncontact monitoring of thickness and drying progress in paint film, Appl. Opt. **44**, 6849 (2005).

[9] C. L. Koch Dandolo and P. U. Jepsen, Wall painting investigation by means of non-invasive terahertz time-domain imaging (THz-TDI): Inspection of subsurface structures buried in historical plasters, J. Infrared, Millimeter, Terahertz Waves **37**, 198 (2016).

[10] C. L. Koch Dandolo, T. Filtenborg, J. Skou-Hansen, and P. U. Jepsen, Analysis of a seventeenth-century panel painting by reflection terahertz time-domain imaging (THz-TDI): Contribution of ultrafast optics to museum collections inspection, Appl. Phys. A **121**, 981 (2015).

[11] J. Bianca Jackson, J. Bowen, G. Walker, J. Labaune, G. Mourou, M. Menu, and K. Fukunaga, A survey of terahertz applications in cultural heritage conservation science, IEEE Trans. Terahertz Sci. Technol. **1**, 220 (2011).

[12] X. Yin, S. Hadjiloucas, B. M. Fischer, B. W.-H. Ng, H. M. Paiva, R. K. H. Galvão, G. C. Walker, J. W. Bowen, and D. Abbott, Classification of lactose and mandelic acid THz spectra using subspace and wavelet-packet algorithms, in

Proceedings of the SPIE 6798, Microelectronics: Design, Technology, and Packaging III, Canberra, ACT, Australia, 679814 (SPIE, 2007).

[13] L. Thrane, R. H. Jacobsen, P. U. Jepsen, and S. R. Keiding, THz reflection spectroscopy of liquid water, Chem. Phys. Lett. **240**, 330 (1995).

[14] C. Rønne, P.-O. Åstrand, and S. R. Keiding, THz spectroscopy of Liquid H_2O and D_2O, Phys. Rev. Lett. **82**, 2888 (1999).

[15] C. Fattinger and D. Grischkowsky, Point source terahertz optics, Appl. Phys. Lett. **53**, 1480 (1988).

[16] M. van Exter, C. Fattinger, and D. Grischkowsky, Terahertz time-domain spectroscopy of water vapor, Opt. Lett. **14**, 1128 (1989).

[17] M. Walther, B. Fischer, M. Schall, H. Helm, and P. U. Jepsen, Far-infrared vibrational spectra of all-trans, 9-cis and 13-cis retinal measured by THz time-domain spectroscopy, Chem. Phys. Lett. **332**, 389 (2000).

[18] J. Neu and C. A. Schmuttenmaer, Tutorial: An introduction to terahertz time domain spectroscopy (THz-TDS), J. Appl. Phys. **124**, 231101 (2018).

[19] B. B. Hu and M. C. Nuss, Imaging with terahertz waves, Opt. Lett. **20**, 1716 (1995).

[20] R. Gente and M. Koch, Monitoring leaf water content with THz and sub-THz waves, Plant Methods **11**, 15 (2015).

[21] R. Gente, A. Rehn, T. Probst, E.-M. Stübling, E. C. Camus, A. A. Covarrubias, J. C. Balzer, and M. Koch, Outdoor measurements of leaf water content using THz quasi time-domain spectroscopy, J. Infrared Milli. Terahz Waves **39**, 943 (2018).

[22] A. Curcio, A. Marocchino, V. Dolci, S. Lupi, and M. Petrarca, Resonant plasma excitation by single-cycle THz pulses, Sci. Rep. **8**, 1052 (2018).

[23] D. Zhang, A. Fallahi, M. Hemmer, X. Wu, M. Fakhari, Y. Hua, H. Cankaya, A.-L. Calendron, L. E. Zapata, N. H. Matlis *et al.*, Segmented terahertz electron accelerator and manipulator (STEAM), Nat. Photonics **12**, 336 (2018).

[24] B. Zaks, R. B. Liu, and M. S. Sherwin, Experimental observation of electron-hole recollisions, Nature (London) **483**, 580 (2012).

[25] O. Schubert, M. Hohenleutner, F. Langer, B. Urbanek, C. Lange, U. Huttner, D. Golde, T. Meier, M. Kira, S. W. Koch *et al.*, Sub-cycle control of terahertz high-harmonic generation by dynamical Bloch oscillations, Nat. Photonics **8**, 119 (2014).

[26] F. Langer, M. Hohenleutner, C. P. Schmid, C. Poellmann, P. Nagler, T. Korn, C. Schüller, M. S. Sherwin, U. Huttner, J. T. Steiner *et al.*, Lightwave-driven quasiparticle collisions on a subcycle timescale, Nature (London) **533**, 225 (2016).

[27] M. Shalaby, C. Vicario, and C. P. Hauri, Simultaneous electronic and the magnetic excitation of a ferromagnet by intense THz pulses, New J. Phys. **18**, 013019 (2016).

[28] N. M. Burford and M. O. El-Shenawee, Review of terahertz photoconductive antenna technology, Opt. Eng. **56**, 010901 (2017).

[29] S. Park, Y. Choi, Y. Oh, and K. Jeong, Terahertz photoconductive antenna with metal nanoislands, Opt. Express **20**, 25530 (2012).

[30] K. Zhong, W. Shi, D. Xu, P. Liu, Y. Wang, J. Mei, C. Yan, S. Fu, and J. Yao, Optically pumped terahertz sources, Sci. China Technol. Sci. **60**, 1801 (2017).

[31] R. Köhler, A. Tredicucci, F. Beltram, H. E. Beere, E. H. Linfield, A. G. Davies, D. A. Ritchie, R. C. Lotti, and F. Rossi, Terahertz semiconductor-heterostructure laser, Nature (London) **417**, 156 (2002).

[32] B. S. Williams, Terahertz quantum-cascade lasers, Nat. Photonics **1**, 517 (2007).

[33] L. Li, L. Chen, J. Zhu, J. Freeman, P. Dean, A. Valavanis, A. G. Davies, and E. H. Linfield, Terahertz quantum cascade lasers with >1 W output powers, Electron. Lett. **50**, 309 (2014).

[34] C. Vicario, B. Monoszlai, and C. P. Hauri, GV/m single-cycle terahertz fields from a laser-driven large-size partitioned organic crystal, Phys. Rev. Lett. **112**, 213901 (2014).

[35] D. J. Cook and R. M. Hochstrasser, Intense terahertz pulses by four-wave rectification in air, Opt. Lett. **25**, 1210 (2000).

[36] A. D. Koulouklidis, C. Gollner, V. Shumakova, V. Y. Fedorov, A. Pugžlys, A. Baltuška, and S. Tzortzakis, Observation of extremely efficient terahertz generation from mid-infrared two-color laser filaments, Nat. Commun. **11**, 292 (2020).

[37] P. González de Alaiza Martínez, I. Babushkin, L. Bergé, S. Skupin, E. Cabrera-Granado, C. Köhler, U. Morgner, A. Husakou, and J. Herrmann, Boosting terahertz generation in laser-field Ionized gases using a sawtooth wave shape, Phys. Rev. Lett. **114**, 183901 (2015).

[38] A. Stathopulos, S. Skupin, and L. Bergé, Terahertz pulse generation by multi-color laser fields with linear versus circular polarization, Opt. Lett. **46**, 5906 (2021).

[39] S. Liu, Z. Fan, C. Lu, J. Gui, C. Luo, S. Wang, Q. Liang, B. Zhou, A. Houard, A. Mysyrowicz *et al.*, Coherent control of boosted terahertz radiation from air plasma pumped by a femtosecond three-color sawtooth field, Phys. Rev. A **102**, 063522 (2020).

[40] V. Vaičaitis, O. Balachninaitė, U. Morgner, and I. Babushkin, Terahertz radiation generation by three-color laser pulses in air filament, J. Appl. Phys. **125**, 173103 (2019).

[41] V. A. Kostin, I. D. Laryushin, and N. V. Vvedenskii, Generation of terahertz radiation by multicolor ionizing pulses, JETP Lett. **112**, 77 (2020).

[42] L. V. Keldysh, Ionization in the field of a strong electromagnetic wave, Zh. Eksperim. i Teor. Fiz. **47**, 1945 (1964) [Sov. Phys. JETP **20**, 1307 (1965)].

[43] J.-F. Daigle, F. Théberge, M. Henriksson, T.-J. Wang, S. Yuan, M. Châteauneuf, J. Dubois, M. Piché, and S. L. Chin, Remote THz generation from two-color filamentation: long distance dependence, Opt. Express **20**, 6825 (2012).

[44] L. Bergé, S. Skupin, R. Nuter, J. Kasparian, and J.-P. Wolf, Ultrashort filaments of light in weakly ionized, optically transparent media, Rep. Prog. Phys. **70**, 1633 (2007).

[45] L. Bergé, K. Kaltenecker, S. Engelbrecht, A. Nguyen, S. Skupin, L. Merlat, B. Fischer, B. Zhou, I. Thiele, and P. U. Jepsen, Terahertz spectroscopy from air plasmas created by two-color femtosecond laser pulses: The ALTESSE project, EPL (Europhys. Lett.) **126**, 24001 (2019).

[46] A. Talbi, B. Zhou, P. U. Jepsen, S. Skupin, A. Courjaud, and L. Bergé, Remote terahertz spectroscopy from extended two-color plasma filaments: The ALTESSE 2 project, EPL (Europhys. Lett.) **143**, 10001 (2023).

[47] V. A. Andreeva, O. G. Kosareva, N. A. Panov, D. E. Shipilo, P. M. Solyankin, M. N. Esaulkov, P. González de Alaiza Martínez, A. P. Shkurinov, V. A. Makarov, L. Bergé *et al.*, Ultrashort terahertz spectrum generation from an air-based filament plasma, Phys. Rev. Lett. **116**, 063902 (2016).

[48] Y. S. You, T. I. Oh, and K. Y. Kim, Off-axis phase-matched terahertz emission from two-color laser-induced plasma filaments, Phys. Rev. Lett. **109**, 183902 (2012).

[49] T. I. Oh, Y. S. You, N. Jhajj, E. W. Rosenthal, H. M. Milchberg, and K. Y. Kim, Intense terahertz generation in two-color laser filamentation: Energy scaling with terawatt laser systems, New J. Phys. **15**, 075002 (2013).

[50] K. Y. Kim, A. J. Taylor, J. H. Glownia, and G. Rodriguez, Coherent control of terahertz supercontinuum generation in ultrafast laser-gas interaction, Nat. Photonics **2**, 605 (2008).

[51] I. Thiele, P. González de Alaiza Martínez, R. Nuter, A. Nguyen, L. Bergé, and S. Skupin, Broadband terahertz emission from two-color femtosecond-laser-induced microplasmas, Phys. Rev. A **96**, 053814 (2017).

[52] A. Gorodetsky, A. D. Koulouklidis, M. Massaouti, and S. Tzortzakis, Physics of the broadband terahertz emission from two-color laser-induced plasma filaments, Phys. Rev. A **89**, 033838 (2014).

[53] A. A. Ushakov, P. A. Chizhov, V. A. Andreeva, N. A. Panov, D. E. Shipilo, M. Matoba, N. Nemoto, N. Kanda, K. Konishi, V. V. Bukin *et al.*, Ring and unimodal angular-frequency distribution of THz emission from two-color femtosecond plasma spark, Opt. Express **26**, 18202 (2018).

[54] I. A. Nikolaeva, N. R. Vrublevskaya, G. E. Rizaev, D. V. Pushkarev, D. V. Mokrousova, D. E. Shipilo, N. A. Panov, L. V. Seleznev, A. A. Ionin, O. G. Kosareva, and A. B. Savel'ev, Terahertz ring beam independent on $\omega - 2\omega$ phase offset in the course of two-color femtosecond filamentation, Appl. Phys. Lett. **124**, 051105 (2024).

[55] E. Hase, J. Degert, E. Freysz, T. Yasui, and E. Abraham, Frequency-resolved measurement of two-color air plasma terahertz emission, J. Eur. Opt. Society-Rapid Publ. **20**, 39 (2024).

[56] M. Kolesik and J. V. Moloney, Nonlinear optical pulse propagation simulation: From Maxwell's to unidirectional equations, Phys. Rev. E **70**, 036604 (2004).

[57] I. Babushkin, S. Skupin, A. Husakou, C. Köhler, E. Cabrera-Granado, L. Bergé, and J. Herrmann, Tailoring terahertz radiation by controling tunnel photoionization events in gases, New J. Phys. **13**, 123029 (2011).

[58] R. J. Noll, Zernike polynomials and atmospheric turbulence, J. Opt. Soc. Am. **66**, 207 (1976).

[59] C. Meng, W. Chen, X. Wang, Z. Lü, Y. Huang, J. Liu, D. Zhang, Z. Zhao, and J. Yuan, Enhancement of terahertz radiation by using circularly polarized two-color laser fields, Appl. Phys. Lett. **109**, 131105 (2016).

[60] C. Tailliez, A. Stathopulos, S. Skupin, D. Buožius, I. Babushkin, V. Vaičaitis, and L. Bergé, Terahertz pulse generation by two-color laser fields with circular polarization, New J. Phys. **22**, 103038 (2020).

[61] L. D. Landau and E. M. Lifshitz, *Quantum Mechanics* (Pergamon, New York, 1965), p. 276.

[62] A. M. Perelomov, V. S. Popov, and M. V. Teret'ev, Ionization of atoms in an alternating electric field, Zh. Eksperim. i Teor. Fiz. **50**, 1393 (1966) [Sov. Phys. JETP **23**, 924 (1966)].

[63] A. V. Borodin, N. A. Panov, O. G. Kosareva, V. A. Andreeva, M. N. Esaulkov, V. A. Makarov, A. P. Shkurinov, S. L. Chin, and X.-C. Zhang, Transformation of terahertz spectra emitted from dual-frequency femtosecond pulse interaction in gases, Opt. Lett. **38**, 1906 (2013).

[64] A. Nguyen, P. González de Alaiza Martínez, J. Déchard, I. Thiele, I. Babushkin, S. Skupin, and L. Bergé, Spectral dynamics of THz pulses generated by two-color laser filaments in air: The role of Kerr nonlinearities and pump wavelength, Opt. Express **25**, 4720 (2017).

[65] R. Boyd, *Nonlinear Optics* (Academic Press, San Diego, 2008).

[66] E. R. Peck and K. Reeder, Dispersion of air, J. Opt. Soc. Am. **62**, 958 (1972).

[67] A. Stathopulos, S. Skupin, and L. Bergé, A Raman-delayed nonlinearity for elliptically polarized ultrashort optical pulses, Eur. Phys. J. Spec. Top. **232**, 2285 (2023).

[68] J. R. Peñano, P. Sprangle, P. Serafim, B. Hafizi, and A. Ting, Stimulated Raman scattering of intense laser pulses in air, Phys. Rev. E **68**, 056502 (2003).

[69] T. A. Pitts, T. S. Luk, J. K. Gruetzner, T. R. Nelson, A. McPherson, S. M. Cameron, and A. C. Bernstein, Propagation of self-focusing laser pulses in atmosphere: Experiment versus numerical simulation, J. Opt. Soc. Am. B **21**, 2008 (2004).

[70] S. Zahedpour, J. K. Wahlstrand, and H. M. Milchberg, Measurement of the nonlinear refractive index of air constituents at mid-infrared wavelengths, Opt. Lett. **40**, 5794 (2015).

[71] M. Kolesik, J. V. Moloney, and M. Mlejnek, Unidirectional optical pulse propagation equation, Phys. Rev. Lett. **89**, 283902 (2002).

[72] A. Kramida, Yu. Ralchenko, J. Reader, and NIST ASD Team, NIST atomic spectra database (version 5.12), [Online], National Institute of Standards and Technology, Gaithersburg, MD, 2024, https://physics.nist.gov/asd.

[73] A. Talebpour, J. Yang, and S. L. Chin, Semi-empirical model for the rate of tunnel ionization in N_2 and O_2 molecule in an intense Ti : Sapphire laser pulse, Opt. Commun. **163**, 29 (1999).

[74] K. Y. Kim, J. H. Glownia, A. J. Taylor, and G. Rodriguez, Terahertz emission from ultrafast ionizing air in symmetry-broken laser fields, Opt. Express **15**, 4577 (2007).

[75] M. Rasmussen, O. Nagy, S. Skupin, A. Stathopulos, L. Bergé, P. U. Jepsen, and B. Zhou, Frequency-resolved characterization of broadband two-color air-plasma terahertz beam profiles, Opt. Express **31**, 9287 (2023).

[76] H. Zhong, N. Karpowicz, and X.-C. Zhang, Terahertz emission profile from laser-induced air plasma, Appl. Phys. Lett. **88**, 261103 (2006).

[77] J. D. Jackson, *Classical Electrodynamics* (Wiley, New York, 1975).

[78] A. Nguyen, P. González de Alaiza Martínez, I. Thiele, S. Skupin, and L. Bergé, THz field engineering in two-color femtosecond filaments using chirped and delayed laser pulses, New J. Phys. **20**, 033026 (2018).

[79] F. Brunel, Harmonic generation due to plasma effects in a gas undergoing multiphoton ionization in the high-intensity limit, J. Opt. Soc. Am. B **7**, 521 (1990).

[80] K.-Y. Kim, Generation of coherent terahertz radiation in ultrafast laser-gas interactions, Phys. Plasmas **16**, 056706 (2009).

[81] L. Bergé, S. Skupin, C. Köhler, I. Babushkin, and J. Herrmann, 3D numerical simulations of THz generation by two-color laser filaments, Phys. Rev. Lett. **110**, 073901 (2013).

[82] S. Akturk, C. D'Amico, M. Franco, A. Couairon, and A. Mysyrowicz, A simple method for determination of nonlinear propagation regimes in gases, Opt. Express **15**, 15260 (2007).

[83] M. Born and E. Wolf, *Principles of Optics* (Pergamon, New York, 1959).

[84] A. A. Ionin, N. G. Iroshnikov, O. G. Kosareva, A. V. Larichev, D. V. Mokrousova, N. A. Panov, L. V. Seleznev, D. V. Sinitsyn, and E. S. Sunchugasheva, Filamentation of femtosecond laser pulses governed by variable wavefront distortions via a deformable mirror, J. Opt. Soc. Am. B **30**, 2257 (2013).

[85] D. V. Apeksimov, Y. E. Geints, A. A. Zemlyanov, A. M. Kabanov, V. K. Oshlanov, A. V. Petrov, and G. G. Matvienko, Controlling TW-laser pulse long-range filamentation in air by a deformable mirror, Appl. Opt. **57**, 9760 (2018).

[86] M. Mlejnek, M. Kolesik, J. V. Moloney, and E. M. Wright, Optically turbulent femtosecond light guide in air, Phys. Rev. Lett. **83**, 2938 (1999).

[87] I. A. Nikolaeva, D. E. Shipilo, N. A. Panov, W. Liu, A. B. Savel'ev, and O. G. Kosareva, Scaling law of THz yield from two-color femtosecond filament for fixed pump power, Photonics **9**, 974 (2022).

[88] C. D'Amico, A. Houard, M. Franco, B. Prade, A. Mysyrowicz, A. Couairon, and V. T. Tikhonchuk, Conical forward THz emission from femtosecond-laser-beam filamentation in air, Phys. Rev. Lett. **98**, 235002 (2007).

[89] C. D. Amico, A. Houard, S. Akturk, Y. Liu, J. Le Bloas, M. Franco, B. Prade, A. Couairon, V. T. Tikhonchuk, and A. Mysyrowicz, Forward THz radiation emission by femtosecond filamentation in gases: Theory and experiment, New J. Phys. **10**, 013015 (2008).

[90] A. V. Balakin, A. V. Borodin, I. A. Kotelnikov, and A. P. Shkurinov, Terahertz emission from a femtosecond laser focus in a two-color scheme, J. Opt. Soc. Am. B **27**, 16 (2010).

[91] J. R. Peñano, P. Sprangle, B. Hafizi, D. Gordon, and P. Serafim, Terahertz generation in plasmas using two-color laser pulses, Phys. Rev. E **81**, 026407 (2010).

[92] M. Clerici, M. Peccianti, B. E. Schmidt, L. Caspiani, M. Shalaby, M. Giguère, A. Lotti, A. Couairon, F. Légaré, T. Ozaki *et al.*, Wavelength scaling of terahertz generation by gas ionization, Phys. Rev. Lett. **110**, 253901 (2013).

[93] C. Köhler, E. Cabrera-Granado, I. Babushkin, L. Bergé, J. Herrmann, and S. Skupin, Directionality of terahertz emission from photoinduced gas plasmas, Opt. Lett. **36**, 3166 (2011).

[94] J. Déchard, A. Nguyen, P. González de Alaiza Martínez, I. Thiele, S. Skupin, and L. Bergé, Validity of the unidirectional propagation model: Application to laser-driven terahertz emission, J. Phys. Commun. **1**, 055009 (2017).

[95] A. M. Bystrov, N. V. Vvedenskii, and V. B. Gildenburg, Generation of terahertz radiation upon the optical breakdown of a gas, JETP Lett. **82**, 753 (2005).

[96] V. B. Gildenburg and N. V. Vvedenskii, Optical-to-THz wave conversion via excitation of plasma oscillations in the tunneling-ionization process, Phys. Rev. Lett. **98**, 245002 (2007).

[97] I. Thiele, B. Zhou, A. Nguyen, E. Smetanina, R. Nuter, K. J. Kaltenecker, P. González de Alaiza Martínez, J. Déchard, L. Bergé, P. U. Jepsen *et al.*, Terahertz emission from laser-driven gas plasmas: A plasmonic point of view, Optica **5**, 1617 (2018).

[98] I. S. Gradshteyn and I. M. Ryzhik, *Table of Integrals, Series, and Products, Eighth Edition* (Academic Press, San Diego, 2014).